PHYSICAL REVIEW C VOLUME 45, NUMBER 5 MAY 1992

Excitation functions for complex fragment emission in the $E/A = 20-100$ MeV $^{14}N + {}^{nat}Ag$, ^{197}Au reactions

J. L. Wile,* D. E. Fields, K. Kwiatkowski, S. J. Yennello, K. B. Morley, E. Renshaw, and V. E. Viola
Departments of Chemistry and Physics and Indiana University Cyclotron Facility, Indiana University, Bloomington, Indiana 47405

C. K. Gelbke, W. G. Lynch, N. Carlin,† H. M. Xu, W. G. Gong, M. B. Tsang, J. Pochodzalla,‡ R. T. deSouza,§ D. J. Fields, and Sam M. Austin
Department of Physics and National Superconducting Cyclotron Laboratory, Michigan State University, East Lansing, Michigan 48824

(Received 16 December 1991)

Excitation functions have been measured for complex fragments with atomic number $Z=3-15$ emitted in collisions of $E/A=20-100$ MeV ^{14}N ions with targets of ^{nat}Ag and ^{197}Au. The results are analyzed in terms of a three-source model which includes: projectilelike fragments from peripheral processes, nonequilibrium emission, and statistical decay of fully equilibrated compound nuclei. Nonequilibrium emission of complex fragments is found to increase rapidly relative to equilibrium emission up to $E/A \approx 60$ MeV and then remain approximately constant thereafter. Evidence for enhanced production of heavier intermediate-mass fragments is found in the data for reactions with the ^{nat}Ag target at energies above $E/A \approx 60$ MeV. Fit parameters for the equilibrium and nonequilibrium sources are examined. In particular, it is observed that the temperature parameter for nonequilibrium emission of complex fragments is independent of bombarding energy up to $E/A = 100$ MeV.

PACS number(s): 25.70.Mn, 25.70.Gh, 25.70.$-$z

I. INTRODUCTION

Studies of complex fragment emission provide an important window through which we can examine the reaction dynamics and subsequent disintegration of highly excited systems formed in nucleus-nucleus collisions at intermediate energies. Of special current interest is the possibility that density and pressure fluctuations at excitation energies approaching the total nuclear binding energy may lead to nuclear instabilities that will be reflected by the properties of these fragments. Thus investigations of complex fragment emission may provide a valuable tool for deducing properties of the nuclear equation of state at low density.

The mechanisms responsible for the formation of intermediate-mass fragments (IMF): $3 \leq Z \lesssim$ fission fragments) can be divided into two general categories: (1) statistical decay from equilibrated heavy residues and (2) nonequilibrium emission on a much faster time scale.

Statistical decay (or very asymmetric fission), which lated near the threshold for IMF emission [1–3] ($E^* \approx 50-100$ MeV) or at backward angles at higher bombarding energies [4–7]. Nonequilibrium emission [4–12] involves fragment emission prior to reaching statistical equilibrium, usually accompanied by preequilibrium light-charged particles or neutrons. The forward-peaked character of this component indicates formation on a time scale considerably shorter than the nuclear equilibration time. Nonequilibrium processes become increasingly important for projectile velocities in the vicinity of the Fermi velocity and above. Studies of asymmetric target-projectile systems suggest that central collisions are primarily responsible for the equilibrium component, whereas nonequilibrium processes originate from more intermediate impact parameters [5,13].

For heavy-ion-induced reactions, projectile remnants (e.g., simple transfer reactions, partially damped collisions, projectile fragmentation, etc.) constitute an additional source which is important at angles near the grazing angle [14,15]. The presently available experimental data suggest that these three mechanisms represent a continuum of reaction-time and impact-parameter-dependent processes, i.e., statistical decay from central collisions, nonequilibrium emission from intermediate impact parameters, and projectile remnants from peripheral collisions [16].

With increasing excitation energy the probability for final states involving two or more IMF's grows significantly. These events are of intense interest at the present time since they are believed to probe instabilities of nuclear matter at very high temperatures. Evidence for this process has been demonstrated at relativistic en-

---

*Present address: Indiana Academy, Ball State University, Muncie, IN 47306.

†Present address: Instituto de Fisica, Universidade de São Paulo, C. Postal 20516, São Paulo, Brazil.

‡Present address: Institut für Kernphysik, Universität Frankfurt, 6000 Frankfurt-am-Main, Germany.

§Present address: Department of Chemistry, Indiana University, Bloomington, IN 47405.

ergies [17–21] and, more recently, in the energy region of interest in this work [22–23]. The definition of the characteristics of multifragment emission and the distinction (if it exists) between sequential statistical decay processes and nonequilibrium multiple breakup modes (multifragmentation) are important questions to be addressed.

Despite the extensive experimental effort that has gone into the study of IMF emission at intermediate energies [26–28], relatively few systematic data sets exist which trace the bombarding energy evolution of these processes from threshold to energies approaching the total nuclear binding energy. In addition to the data reported here, other systems for which IMF production has been investigated over a significant range of bombarding energies, with relatively low detector thresholds and good angular coverage, include the following: the $^{18}O+^{nat}Ag$, ^{197}Au reactions between $E/A=30$ and 84 MeV [12], $^{12}C+^{197}Au$ from $E/A=30$ to 1200 MeV [29], $^{20}Ne+^{nat}Ag$, ^{197}Au from $E/A=20$ to 60 MeV [30], and $^{3}He+^{nat}Ag$ from $E/A=15$ to 1200 MeV [1,4,31]. Proton-induced IMF emission has been studied on medium-mass target nuclei (Ag,Xe) from 160 MeV to 80 GeV [7,20,32], although with limited angular coverage at energies above 500 MeV. In addition, the $^{139}La+^{12}C$ reaction has been studied from $E/A=50$ to 100 MeV [33], but does not cover the IMF mass range below $Z\cong 8$.

The objective of the research reported here has been to perform a systematic set of inclusive IMF excitation function measurements with low detector thresholds and angular coverage from 20° to 160°. The systems studied were the $^{14}N+^{nat}Ag$ and ^{197}Au reactions between $E/A=20$ and 100 MeV. These data are intended to provide a qualitative overview of the mechanisms responsible for IMF emission as the projectile energy is increased from the threshold region, across the Fermi energy, and eventually approaches the total nuclear binding energy. In addition, the results should provide a useful characterization of IMF properties that are necessary for interpretation of data from more complex exclusive experiments. Preliminary reports of these results have been presented in Refs. [6] and [34].

II. EXPERIMENTAL PROCEDURES

Two experiments were carried out at the National Superconducting Cyclotron Laboratory (NSCL) at Michigan State University (MSU).

The first [6] utilized beams of $E/A=20$, 30, 40, and 50 MeV from the NSCL K500 cyclotron in the 152-cm-diam scattering chamber. Beam currents ranged from 25 to 70 electrical nA, as measured by a Faraday cup, assuming complete stripping in the target. The beam spot size was approximately 3 mm×3 mm. Self-supporting, high-purity targets of ^{nat}Ag (1.48 mg/cm^2) and ^{197}Au (1.16 mg/cm^2) were bombarded. Carbon and blank targets were also studied to monitor any possible sources of contamination due to carbon buildup or beam halo. The target thicknesses were determined both by weight and by measuring the energy loss of α particles from an ^{241}Am source in the target material. IMF's were detected at angles of 60°, 90°, 120°, and 165° with four fixed detector telescopes. A movable telescope was used to acquire data at forward angles of 20°, 30°, and 40°. The solid angles and components of these detectors are listed in Table I.

The second experiment was performed with beams of $E/A=60$, 80, and 100 MeV from the K1200 cyclotron at NSCL. Beam currents were 5–25 nA, and the beam spot size was less than 5×5 mm^2. Bombardments of high-purity 1.31-mg/cm^2 ^{nat}Ag and 0.93-mg/cm^2 ^{197}Au targets were carried out in the 234-cm-diam scattering chamber. In this experiment six fixed-angle detector telescopes were employed along with a movable telescope, which sampled data at 20° and 35°. The solid angles and basic telescope arrangement are also listed in Table I. The performance of the large solid-angle detectors is described more fully in Ref. [35]. The energy threshold for these detector telescopes was approximately $E_{\mathrm{thres}}\lesssim 0.5$ MeV/nucleon. In this paper we discuss only the data for IMF charge distributions; results for Z- and A-identified nuclide distributions and light-charged-particle spectra are planned to be presented in subsequent reports.

In both experiments sufficient data were taken for background determination using both a blank frame and

TABLE I. Detector characteristics for $E/A=20–100$ MeV ^{14}N bombardments. GIC is the axial-field gas ionization chamber, Si(SB) is the surface-barrier silicon detector, Si(IP) is the ion-implanted silicon detector, Si(Li) is the lithium-drifted silicon detector, and CsI(Tl) is the thallium-activated cesium iodide scintillator.

Angle	Solid angle (msr)	Telescope components
		$E/A=20–50$ MeV ^{14}N bombardments
20°,30°,40°	1.66	30 μm Si(SB)/100 μm Si(SB)/400 μm Si(SB)/5 mm Si(Li)
60°	2.66	GIC at 18 Torr CF$_4$/300 μm SI(SB)/5 mm Si(Li)
90°,120°,165°	4.6	GIC at 18 Torr CF$_4$/300 μm SI(SB)/5 mm SI(Li)
		$E/A=60–100$ MeV ^{14}N bombardments
20°,35°	0.67	GIC at 20 Torr CF$_4$/75 μm Si(SB)/300 μm Si(SB)/5 mm Si(Li)/5 mm Si(Li)
50°	1.86	GIC at 20 Torr CF$_4$/70 μm Si(SB)/700 μm Si(SB)/5 mm Si(Li)
70°	16.9	GIC at 20 Torr CF$_4$/225 μm Si(IP)/501 μm Si(IP)
90°	16.9	GIC at 17 Torr CF$_4$/226 μm Si(IP)/500 μm Si(IP)/25 mm CsI(Tl)
120°	16.9	GIC at 17 Torr CF$_4$/228 μm Si(IP)/25 mm CsI(Tl)
140°	16.9	GIC at 17 Torr CF$_4$/226 μm Si(IP)/301 μm Si(IP)
160°	16.9	GIC at 17 Torr CF$_4$/229 μm Si(IP)/25 mm CsI(Tl)

a carbon target. The blank target showed no appreciable count rate from nontarget sources. The detected fragments from the carbon targets were predominantly below the energy region of interest for the ${}^{\mathrm{nat}}$Ag and ^{197}Au targets and therefore carbon contamination on the gold and silver targets would have been distinctive. Because of these cross-checks, the carbon contamination was determined to be negligible.

The energy calibrations of the ion chambers were obtained by determining the energy loss at several gas pressures with respect to the energy signal in the corresponding silicon detector. System linearities were checked with a charge-injecting pulser calibrated with an ^{241}Am alpha source. The calibrations for the silicon detectors were obtained in a similar manner using a full alpha energy (corrected for source window energy loss) after removing the gas and front window of the ion chambers for the ΔE detectors. Separate calibrations were performed for the Si(Li) detectors. Silicon detector energy calibrations were cross-checked against various detectors and against the punch-through energies of the light-penetrating particles. Final particle energies were corrected for energy loss in the ion chamber window material and on half the target thickness.

Data acquisition and on-line analysis at MSU were performed using the NSCL networked CAMAC/VME data-acquisition system. Final data analysis at Indiana University Cyclotron Facility (IUCF) used an updated version of the XSYS data-reduction program [36].

III. EXPERIMENTAL RESULTS

The major objective of this work was to examine the systematic trends that characterize IMF production at intermediate energies. In this section we present representative data that describe the energy spectra, angular distributions, charge distributions, and cross sections for $Z=3-15$ fragments as a function of ^{14}N bombarding energy for a medium-mass (${}^{\mathrm{nat}}$Ag) and a heavy-mass target nucleus (^{197}Au). The data set defines the behavior of the equilibrium and nonequilibrium yields nearly completely, but only partially covers the quasielastic and partially damped component of the spectra. The reader is referred to the work of Kiss et al. [37] for a more complete description of these projectilelike yields in similar systems. The data are subsequently examined in terms of a moving-source model with three components. The emphasis in this paper is on the systematic experimental features of the data.

Representative fragment kinetic-energy spectra, shown in Figs. 1–4, illustrate the dependence of the spectral shapes on projectile energy, angle of emission, and IMF atomic number. In Fig. 1 energy spectra for Be fragments emitted in the $E/A=80$ MeV ${}^{14}\mathrm{N}+{}^{\mathrm{nat}}\mathrm{Ag}$ reaction are presented. The Be spectra are typical for fragments with $Z\leq 7$ at all energies, except for the appearance of quasielastic peaks for nitrogen and carbon fragments near the grazing angle. The forward-angle spectra exhibit a peak in the vicinity of the Coulomb energy, followed by a flat tail that extends up to energies for which the fragment E/A value is near that of the projectile. The tail is associated with projectile remnants arising from peripheral interactions, as demonstrated by coincidence experiments involving events tagged according to linear momentum transfer [38,39]. As the emission angle increases, the spectral slopes become increasingly steep, until at backward angles they are approximately consistent with those expected for evaporation from an equilibrated compound nucleus formed following preequilibrium light-particle emission.

For ejectiles with $Z>7$, where projectilelike fragments do not contribute appreciably to the fragment yields, the energetic flat portion of the fragment kinetic-energy distribution disappears. This is demonstrated in Fig. 2 for Ne ejectiles from the reaction of $E/A=80$ MeV ^{14}N ions with ^{197}Au. However, at forward angles, the slope of the spectral tails is much flatter than expected for emission from an equilibrated complete fusion residue. As with the lighter fragments, the spectral shapes approach the compound-nucleus expectation at backward angles. Thus the shapes of the $Z>7$ spectra strongly resemble those for nucleon emission from intermediate-energy light-ion-induced reactions [40,41]. It is important to note that

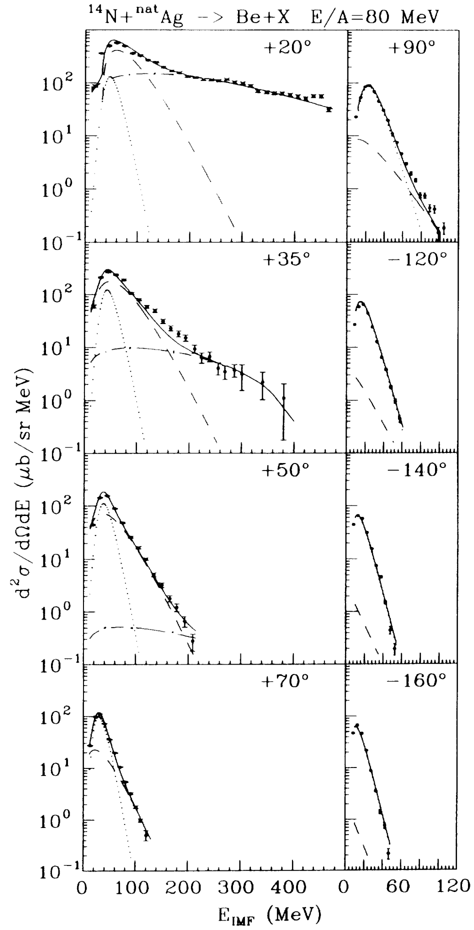

FIG. 1. Kinetic-energy spectra of $Z=4$ fragments from the $E/A=80$ MeV ${}^{14}\mathrm{N}+{}^{\mathrm{nat}}\mathrm{Ag}$ reaction at angles indicated in figure. Fit components are described as follows: equilibrium source (dotted line), nonequilibrium source (dashed line), projectilelike source (dot-dashed line), and total (solid line).

characterization of the backward-angle spectra is extremely important in performing moving-source decomposition of the data, as will be discussed in the following section. Although not explicitly shown in these figures, the data also illustrate the previously observed [1,4] shape evolution of the backward-angle spectra as a function of increasing fragment charge, i.e., from Maxwellian shapes for low-Z fragments to Gaussian distributions for the heaviest fragments.

The dependence of the fragment energy spectra on projectile bombarding energy is presented in Figs. 3 and 4 for several representative angles. Figure 3 illustrates the behavior of fragments lighter than the projectile, i.e., boron ($Z=5$) fragments from the $^{14}\mathrm{N}+{}^{197}\mathrm{Au}$ reaction. At forward angles a shoulder in the spectra just below the E/A value of the beam is prominent at the lowest energies, but disappears as the beam energy is increased. This behavior is correlated with the corresponding decrease in the grazing angle for the reaction as a function of increasing bombarding energy; hence, at the higher energies, peripheral processes are concentrated at very small angles that are not covered by our detector geometry. At intermediate angles the spectra exhibit the standard Maxwellian pattern for IMF's: a distinct maximum near the Coulomb repulsion energy for binary breakup, followed by an exponential tail with slopes corresponding to temperatures well in excess of that for an equilibrated complete fusion residue. In contrast, the backward-angle spectra at all energies exhibit spectra approximately consistent with those expected for compound nucleus decay following preequilibrium light particle emission.

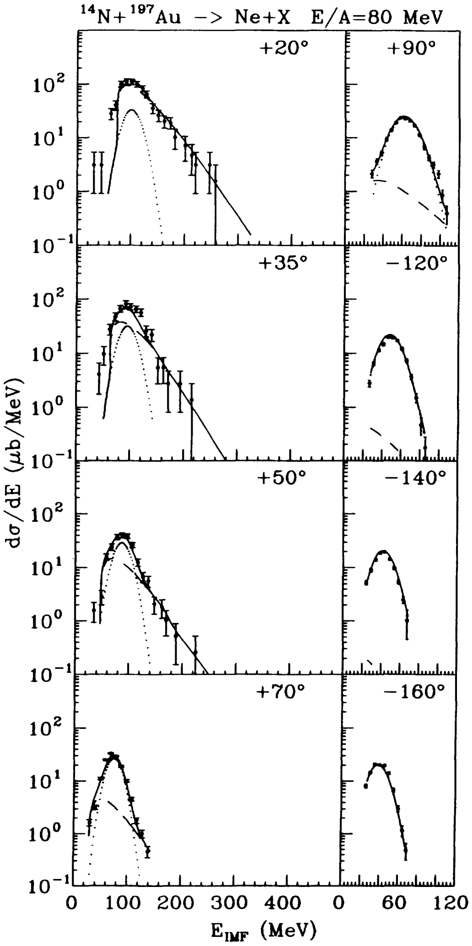

FIG. 2. Kinetic-energy spectra of $Z=10$ fragments from the $E/A=80$ MeV $^{14}\mathrm{N}+{}^{197}\mathrm{Au}$ reaction at angles indicated in figure. Fit components are same as in Fig. 1.

In Fig. 4 the data for sodium fragments ($Z=11$) from the $^{14}\mathrm{N}+{}^{\mathrm{nat}}\mathrm{Ag}$ reaction are shown. These spectra differ from the general pattern observed in Fig. 3 in two respects. First, the projectile remnant component is absent in all spectra, a consequence of the low probability for $Z>7$ ejectiles and the very small grazing angle for this system. Second, there appears to be a systematic broadening of the Coulomb peak toward lower fragment kinetic energies as the projectile energy increases. This behavior is most apparent for the heaviest fragments from the $^{\mathrm{nat}}\mathrm{Ag}$ target; it is not readily discernible for reactions induced on $^{197}\mathrm{Au}$ (cf. Fig. 2). Similar behavior has been observed in excitation function studies of the $^{12}\mathrm{C}+{}^{197}\mathrm{Au}$ [29] and $^{3}\mathrm{He}+{}^{\mathrm{nat}}\mathrm{Ag}$ [31] systems at comparable total bombarding energies. Since the effect is present for IMF's emitted in the forward hemisphere, it is unlikely to be associated with kinematic effects. Instead, the results are suggestive of significant distortions of the Coulomb field of emitting source and/or the emission from a very broad distribution of source charges following multiple light-charged-particle or IMF emission. An important consequence of this contribution to the $^{\mathrm{nat}}\mathrm{Ag}$ spectra is to enhance the cross sections of heavy IMF's significantly for bombarding energies above $E/A\approx60$ MeV (see discussion of excitation functions below).

One of the most notable features of the bombarding energy dependence of the IMF kinetic-energy distribution is that once one is well above the threshold region ($E/A\approx20$ MeV), all spectra at a given angle are remarkably similar, both in shape and absolute magnitude, except for the Coulomb peak distortions for $^{\mathrm{nat}}\mathrm{Ag}$ discussed above. It should be noted that for the $^{14}\mathrm{N}+{}^{\mathrm{nat}}\mathrm{Ag}$ system, the backward-angle spectral peaks are not fully measured for beam energies $E/A>50$ MeV and $Z\gtrsim8$ because of kinematic shifts and detector thresholds. With respect to the moving-source fits discussed below, this limitation is compensated for by performing measurements at several angles, especially in the backward hemisphere—thus constraining the fits with the systematic kinematic shifts of the spectral tails for $\theta\gtrsim90°$ and the location of the Coulomb peaks for $\theta\lesssim90°$. (Note also that the angles shown in Figs. 3 and 4 are slightly different for bombarding energies above and below $E/A=50$ MeV.)

Laboratory angular distributions are shown in Figs. 5 and 6 for representative ejectiles and bombarding energies. The points represent measured differential cross sections and do not include extrapolations due to unmeasured energies below our detector thresholds, which influences the data points for large Z values. In the forward hemisphere the differential cross sections increase exponentially with decreasing angle of emission, with little dependence on IMF charge, target nucleus, or projectile energy. Coincidence studies at $E/A=35$ MeV have shown that outside the grazing angle, these ejectiles are associated with large linear momentum transfers from projectile to target (~70% on average) [5]. This fact, combined with the strong forward peaking of the cross sections, indicates that a major source of these fragments involves nonequilibrium emission from the composite system. At angles near the grazing angle, an even steeper cross section increase is observed (note, for example, oxygen fragments from the $E/A=20$ MeV $^{14}N+^{nat}Ag$ reaction in Fig. 5). Coincidence studies of these fragments [38,39] show that they arise from interactions involving small linear momentum transfers ($\lesssim 20\%$). Hence these ejectiles appear to be associated with peripheral processes, e.g., simple transfer reactions, partially damped events, and projectile fragmentation.

In contrast, the laboratory angular distributions in the backward hemisphere are relatively isotropic. In some cases, especially at lower energies and for heavier fragments, an increase is observed in the yields near 180°. This pattern resembles binary fission from an equilibrated, rotating compound nucleus. Such an interpretation is also supported by linear-momentum-transfer measurements in coincidence with IMF's emitted at backward an-

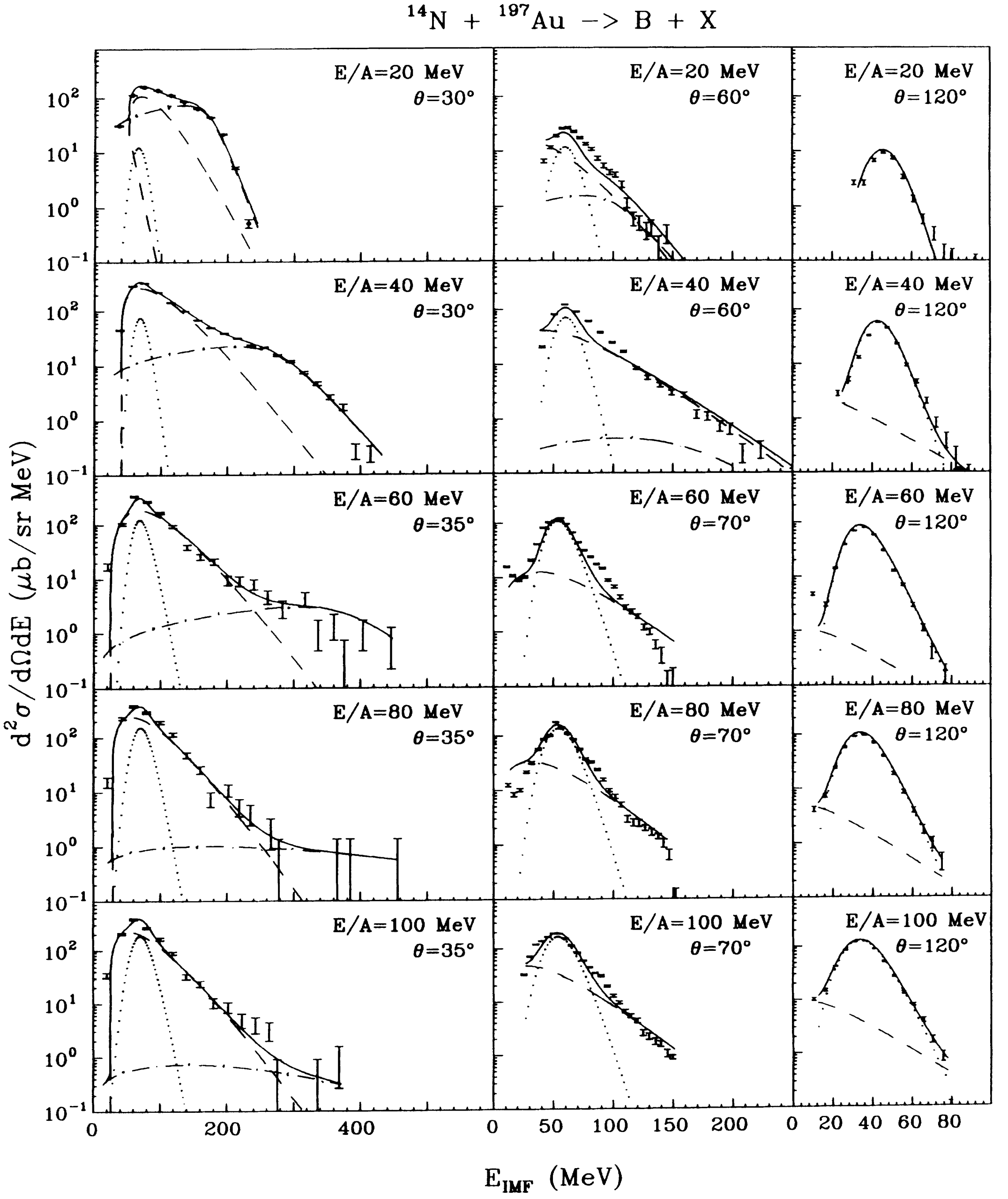

FIG. 3. Kinetic-energy spectra of $Z=5$ fragments from the $^{14}N+^{197}Au$ reaction at forward (30° or 35°), intermediate (60° or 70°), and backward angles (120°). Data are shown for ^{14}N bombarding energies of $E/A=20$, 40, 60, 80, and 100 MeV. Fit components are same as in Fig. 1.

gles [5], which show that IMF's are emitted from composite system which involve nearly complete linear momentum transfer, at least below $E/A \lesssim 50$ MeV [5,42]. At higher bombarding energies one expects the fractional linear momentum transfer to decrease due to the growth of nonequilibrium light-particle emission.

In summary, the qualitative features of the IMF kinetic-energy spectra and angular distributions argue for at least three mechanisms for IMF formation in the $E/A=20-100$ MeV regime: (1) projectile remnants from peripheral interactions, (2) nonequilibrium emission on a fast time scale, and (3) binary decay of a nearly equilibrated heavy residue. Coincidence measurements which define the linear momentum transfer of the emitting source support this picture [5,39,40,43]. Clearly, this is a schematic model that represents a continuum of time- and impact-parameter-dependent processes.

IV. MOVING-SOURCE FITS

In order to assess the relative contributions of the three emission mechanisms proposed in the previous section,

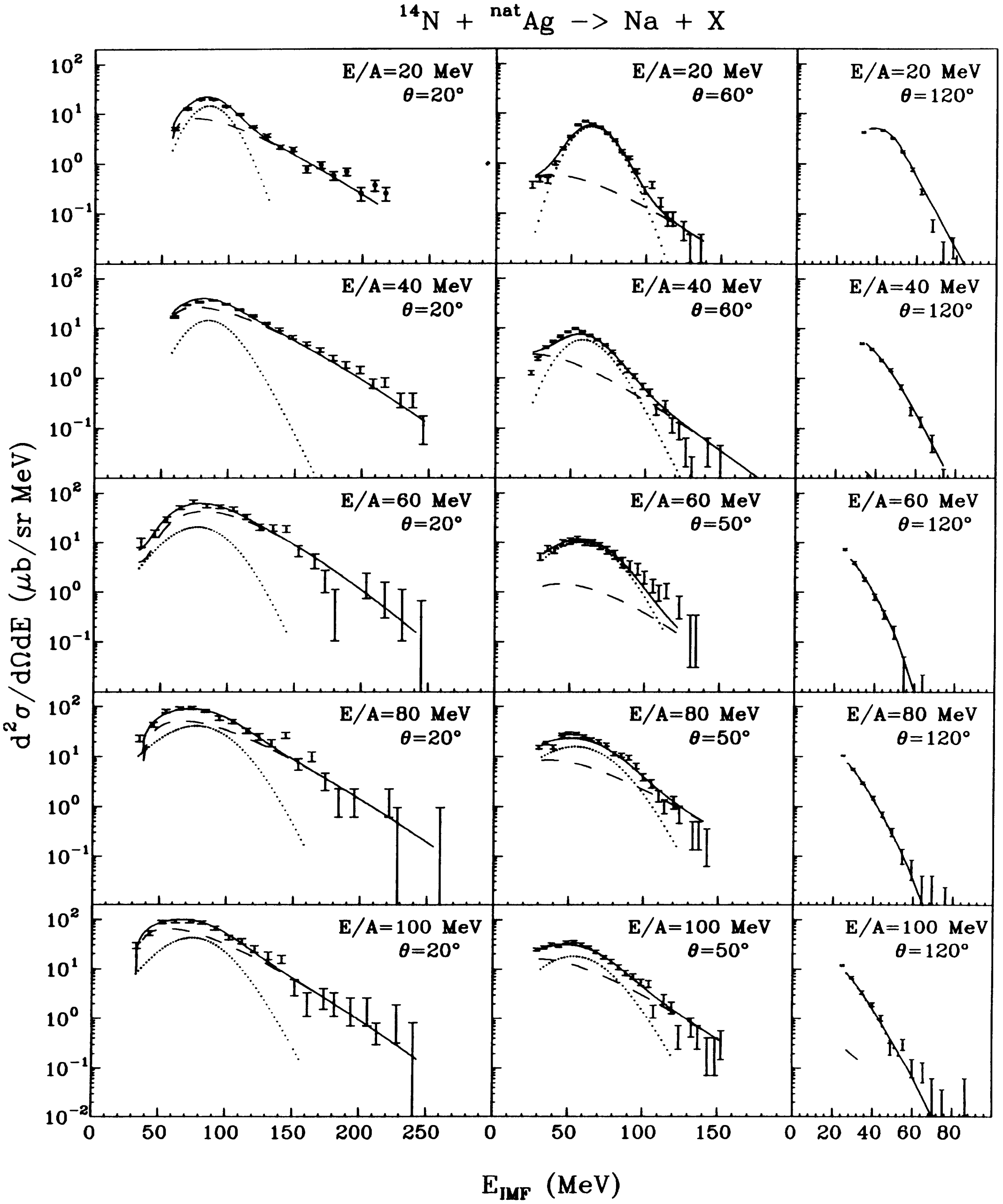

FIG. 4. Kinetic-energy spectra of $Z=11$ fragments from the $^{14}N+^{nat}Ag$ reaction at forward (20°), intermediate (50° or 60°), and backward angles (120°). Data are shown for ^{14}N bombarding energies of $E/A=20$, 40, 60, 80, and 100 MeV. Fit components are same as in Fig. 1.

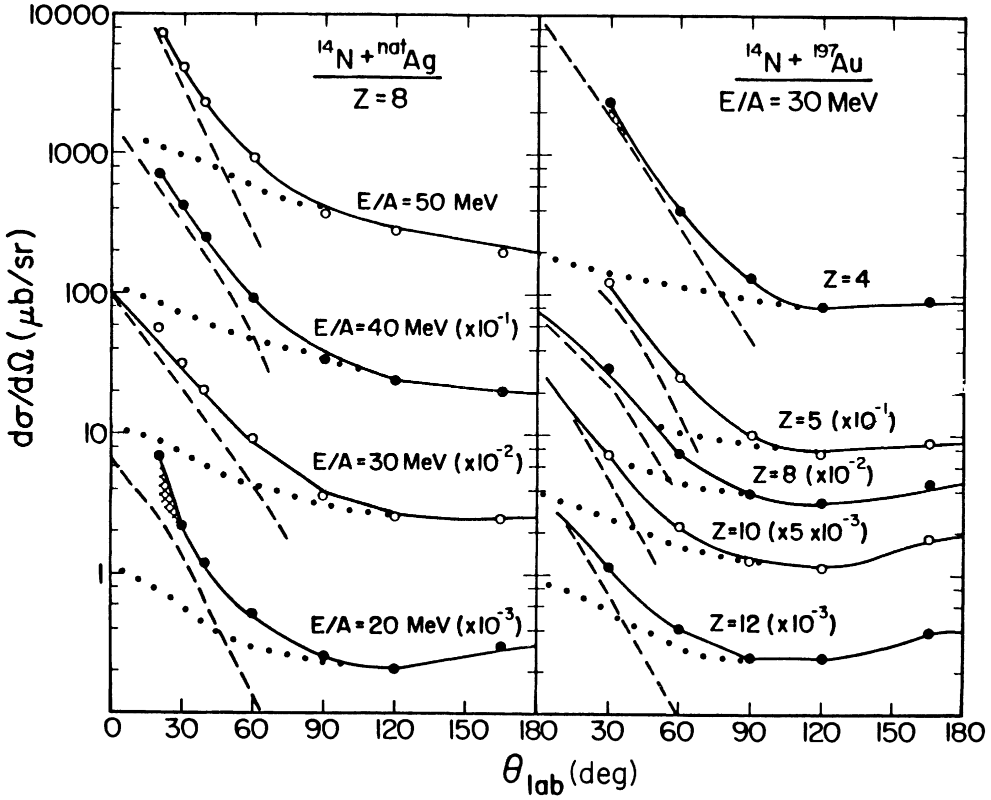

FIG. 5. Representative angular distributions for (left frame) $Z=8$ fragments from $^{14}N+^{nat}Ag$ reaction at $E/A=20$, 30, 40, and 50 MeV and (right frame) for $Z=4$, 5, 8, 10, and 12 from the $E/A=30$ MeV ^{14}N reaction. (Data not corrected for detector thresholds.) Fit components are same as in Fig. 1.

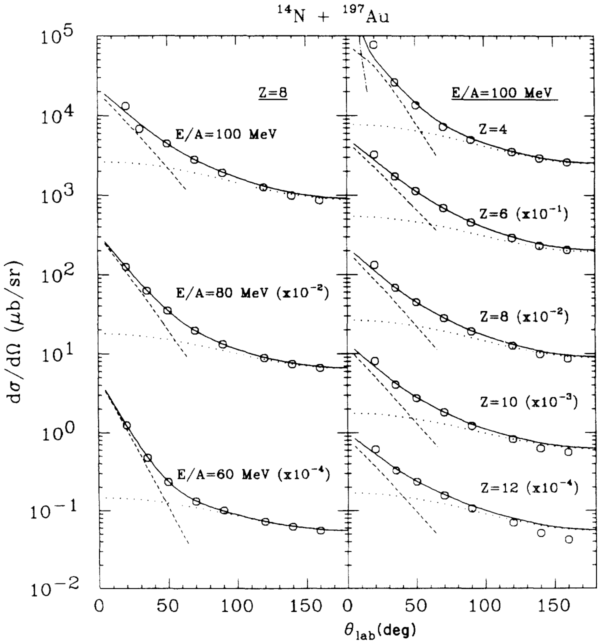

FIG. 6. Representative angular distributions for (left frame) $Z=8$ fragments from the $^{14}N+^{197}Au$ reaction at $E/A=60$, 80, and 100 MeV and (right frame) for $Z=4$, 6, 8, 10, and 12 for the $E/A=100$ MeV reaction. (Data not corrected for detector thresholds.) Fit components are same as in Fig. 1.

we have performed a simultaneous three-source fit to the energy spectra at all angles. This schematic decomposition represents an oversimplification of the continuum of processes that must necessarily contribute to the total IMF yields. In addition, multifragment emission is not considered as an explicit source in the decomposition. Although such processes have been identified in similar systems at these bombarding energies [22–25] and may well contribute significantly at the highest bombarding energies, for the present purposes they can be considered as higher-multiplicity forms of the sources already defined.

The equilibrium source was assumed to be the binary decay of a targetlike residue formed in central collisions for which the interaction time is greater than approximately one nuclear rotation period—therefore leading to a forward-backward symmetric angular distribution. This is a necessary, but not sufficient, condition for emission from a fully equilibrated system, since the time scale for full equilibration may exceed the rotation period for these systems.

The equilibrium source was schematically characterized by a mean velocity v_{eq}, Coulomb barrier B_{eq}, and temperature T_{eq}. The spectral shapes were parametrized according to the scission-point model of Nix [43], modified to account for mass asymmetric systems by Moretto [44],

$$P(E) \propto (2E-p)e^{-E/T}\operatorname{erf}\left[(p-2E)/2\sqrt{pT}+2\left[\frac{pT}{\pi}\right]^{1/2} e^{-(p^2+4E^2)/4pT}\right], \tag{1}$$

which introduces an additional parameter p, a Z-dependent amplification parameter which permits the evolution of spectral shapes with fragment charge. In addition, the angular distribution function was assumed to be symmetric about 90° in the emitting-source frame and described by a function $w(\theta) \propto (1+\alpha\cos^4\theta)$, where the anisotropy α is a fit parameter. This latter parameter is essential at lower energies in order to account empirically for angular momentum effects which produce anisotropy in the angular distribution near 180° (see Fig. 5). The sensitivity of the equilibrium cross sections to the backward-angle data illustrates the importance of performing measurements with low-energy thresholds at several angles in the backward hemisphere. This component is described by the dotted lines in Figs. 1–6.

Whereas the procedures for describing equilibrium emission are relatively well defined from low-energy studies, the mechanism for nonequilibrium emission is much more complex and remains poorly understood. Because of the close coupling of the reaction dynamics and IMF emission process, a quantitative description of these processes is not yet available. Therefore, for this initial analysis, we employ a phenomenological approach [45,46] in which IMF's are assumed to be emitted from the nuclear surface with a Maxwellian energy distribution

$$P(e) \propto (E-B_{\mathrm{neq}})\exp\{-(E-B_{\mathrm{neq}})/T_{\mathrm{neq}}\}, \tag{2}$$

from a moving source with average velocity v_{neq} and characterized by a spectral slope T_{neq} and Coulomb barrier B_{neq}. An empirical angular distribution function of the form $w(\theta) \propto \exp(-b\theta)$ in the center-of-mass reference frame was added in the fitting routine [40,41]. This term was found to have a significant effect in lowering the χ^2/N DF (degrees of freedom) values of the fit compared to an isotropically emitting source. Improvement in the fits was most notable at intermediate angles in the energy region between the Coulomb peak and exponential tail of the spectra. However, even with this improvement, there is still a noticeable underprediction of the data at intermediate angles for many spectra. Because of the uncertainties inherent in the underlying physics responsible for the nonequilibrium component, the extracted values of v_{neq}, T_{neq}, and B_{neq} (see Appendix) should not be interpreted literally. Rather, these are fit parameters that integrate over a continuum of processes which occurs over a time interval that extends from the collision time to that for nearly complete thermalization.

Borderie *et al.* [47] have proposed that the nonequilibrium fragments have their origin in damped (deep inelastic) collisions. However, several arguments support the nonequilibrium classification as a distinct mechanism, i.e., one in which nucleon-nucleon collisions destroy the memory of all projectile properties, other than the beam direction, rather than one dominated by nucleon exchange between projectilelike and targetlike fragments. This point of view is supported by the following: (1) the strong correspondence of these inclusive IMF energy, angular, and charge distributions with those observed in light-ion-induced reactions, where damped processes are absent [1,4,7], (2) IMF charge and mass distributions which decrease according to a power law $\sigma(Z) \propto Z^{-\tau}$ rather than being peaked near the Z and A of the projectilelike and targetlike fragments, and (3) kinetic-energy spectra which are peaked near the value for touching Coulomb spheres and then decrease exponentially, rather than being peaked near the E/A of the beam and decreasing with decreasing energy. The nonequilibrium component of the fits is given by the dashed lines in Figs. 1–6.

In order to account for the sharply rising angular distributions and rapid increase in yield for fragments with energies near the E/A value of the beam at very forward angles, a third source is introduced into our fitting routine. This source integrates the effects of projectile remnants produced in transfer reactions, partially damped collisions, and projectile fragmentation. For some range of (large) impact parameters, this component of the IMF ejectile distribution must evolve into the nonequilibrium component, depending on projectile mass and energy. The projectilelike source has been parametrized here according to the schematic prescription of Kiss *et al.* [37] and is important primarily for fragments with $Z \le 8$ at very forward angles and for the lower bombarding energies where the grazing angle is relatively large. The center-of-mass functional form of this component was given by

$$P(E) \propto \sqrt{E/A}\, e^{-B\sqrt{E/A}}\left(1+e^{[(E/A)-E_0/A]C}\right)^{-1}, \tag{3}$$

where E/A refers to the energy and mass of the IMF and B, C, and E_0 are fit parameters. In addition, an angular distribution of the form $W(\theta) \propto \exp(-D\theta)$ was assumed, where D is an additional fit parameter. A total of five parameters are used in this fit component. Because of the limited range of forward angles covered in this experiment, our principal goal in treating this component was to minimize its distortion of the nonequilibrium spectra. For a more complete description of the physics of these peripheral processes, the reader is referred to Refs. [14], [15], and [38]. The projectile remnant component of our fits is shown by the dot-dashed lines in Fig. 1–6.

Simultaneous fits were performed for each atomic number at each bombarding energy for the measured IMF triply differential cross sections $d^3\sigma/d\Omega\, dE\, dZ$ at all angles. Error analysis is described in the Appendix. The fits included 14 parameters and 3 normalizations. Average fit parameters are tabulated in Tables II and III for the $^{\mathrm{nat}}$Ag and ^{197}Au targets, respectively. Examination of the spectra and angular distributions in Figs. 1–6 demonstrates the quality of the total fits, given by the solid line. In general, χ^2 values based on statistical errors

TABLE II. Ratio of IMF cross section from targetlike source to total reaction cross section [36] and average fit parameters for ^{14}N+$^{\rm nat}$Ag as a function of bombarding energy.

	E/A (MeV)						
	20	30	40	50	60	80	100
$\sigma_{\rm IMF}/\sigma_R$	0.059	0.100	0.13	0.14	0.15	0.23	0.27
$\langle T_{\rm eq}\rangle$ (MeV)	4.9	5.0	5.10	5.3	5.9	6.5	7.1
$\langle v_{\rm eq}\rangle/v_{\rm CN}$	0.93	0.87	0.78	0.68	0.67	0.64	0.56
$\langle B_{\rm eq}\rangle/B_{\rm CN}$	0.96	0.91	0.86	0.76	0.64	0.58	0.56
$\langle T_{\rm neq}\rangle$ (MeV)	16.8	20.0	18.7	17.9	16.6	17.6	18.6
$\langle v_{\rm neq}/v_{\rm beam}$	0.27	0.23	0.24	0.21	0.18	0.15	0.14
$\langle B_{\rm neq}\rangle/B_{\rm CN}$	0.25	0.23	0.16	0.16	0.11	0.12	0.076
$\sigma_{\rm tot}$ (mb)	155	291	366	389	418	611	684

were between 0.5 and 1.5. While overall the fits are quite satisfactory, for some systems at intermediate angles the fitting routine underestimates the observed yields for fragment energies in the region where the equilibrium component merges with the nonequilibrium exponential tail. The fitting functions have been integrated over all fragment energies and angles to yield cross sections for equilibrium emission, $\sigma_{\rm eq}(Z)$; nonequilibrium emission, $\sigma_{\rm neq}(Z)$; and the sum of these, $\sigma_{\rm tot}(Z)$. Values for $\sigma_{\rm tot}(Z)$ are given in Tables IV and V.

Figure 7 presents the excitation functions for fragments with even Z for equilibrium emission, $\sigma_{\rm eq}(Z)$; nonequilibrium emission, $\sigma_{\rm neq}(Z)$; and the sum of equilibrium plus nonequilibrium emission, $\sigma_{\rm IMF}(Z)$ (tabulated in Tables IV and V). Sums were performed over fragments with $Z=3-15$ inclusive and include extrapolations to data below the detector thresholds based on the equilibrium component of the fit. Also shown in Fig. 7 are the calculated cross sections σ_R according to the prescription of Kox *et al.* [48]. The excitation functions for odd-Z elements exhibit behavior similar to those for even Z, except that the Li ($Z=3$) yields are systematically a factor of approximately 3 larger than for beryllium ($Z=4$).

The excitation functions are slightly different for the two projectile-target combinations. For the ^{197}Au target the cross sections increase monotonically as a function of bombarding energy for both components and the total. Equilibrium emission for all Z values increases rapidly between $E/A=20$ and 30 MeV and then continues a uniform increase up to the maximum energy measured. The nonequilibrium component, on the other hand, increases in yield in a Z-dependent fashion. The yields of light nonequilibrium IMF's grow rapidly up to about $E/A=40$ MeV and then become essentially independent of bombarding energy thereafter; these saturation cross sections for $\sigma_{\rm neq}(Z)$ are distinctly higher than the corresponding $\sigma_{\rm eq}(Z)$ values, except at the highest bombarding energies. For the heavier IMF's, $\sigma_{\rm neq}$ saturates near $E/A=60$ MeV at values slightly smaller than the corresponding $\sigma_{\rm eq}(Z)$ values. We discuss this behavior below in terms of the ratios $\sigma_{\rm neq}(Z)/\sigma_{\rm tot}(Z)$.

For the $^{\rm nat}$Ag target the excitation function systematics are more complex. Because of the lower Coulomb barriers for this system, the equilibrium yields are already substantial at $E/A=20$ MeV. The values of $\sigma_{\rm eq}(Z)$ for the lightest fragments increase monotonically over the entire energy region, with perhaps a slight enhancement above $E/A=60$ MeV. For heavier IMF's, however, the equilibrium cross sections are approximately constant up to $E/A=60$ MeV and then show a distinct Z-dependent increase above this energy. The nonequilibrium excitation functions continue to rise uniformly over the entire energy range, with the slope becoming steeper with in-

TABLE III. Ratio of IMF cross section from targetlike source to total reaction cross section [36] and average fit parameters for ^{14}N+^{197}Au as a function of bombarding energy.

	E/A (MeV)						
	20	30	40	50	60	80	100
$\sigma_{\rm IMF}/\sigma_R$	0.040	0.10	0.16	0.19	0.22	0.24	0.28
$\langle T_{\rm eq}\rangle$ (MeV)	3.5	4.3	4.3	4.9	4.9	5.3	5.7
$\langle v_{\rm eq}\rangle/v_{\rm CN}$	0.99	0.99	0.93	0.87	0.87	0.80	0.76
$\langle B_{\rm eq}\rangle/B_{\rm CN}$	1.00	1.00	0.98	0.95	0.88	0.86	0.85
$\langle T_{\rm neq}\rangle$ (MeV)	14.6	20.5	19.4	17.6	21.5	21.7	21.6
$\langle v_{\rm neq}\rangle/v_{\rm beam}$	0.35	0.28	0.26	0.23	0.16	0.12	0.099
$\langle B_{\rm neq}\rangle/B_{\rm CN}$	0.30	0.30	0.25	0.23	0.29	0.37	0.35
$\sigma_{\rm tot}$ (mb)	127	356	558	664	791	864	933

TABLE IV. Cross sections for IMF production from targetlike source, $\sigma_{\text{tot}}(Z)=\sigma_{\text{eq}}(Z)+\sigma_{\text{neq}}(Z)$, for the $^{14}\text{N}+^{\text{nat}}\text{Ag}$ reaction as a function of bombarding energy. Statistical plus systematic errors from about 10% for $Z=3$ fragments to 20% for $Z=15$.

				E/A (MeV)			
$\sigma_{\text{tot}}(Z)$ (mb)	20	30	40	50	60	80	100
3	55	123	154	165	186	247	262
4	20	37	50	55	55	72	84
5	24	38	50	55	53	81	90
6	27	35	44	45	42	64	77
7	14	19	22	22	24	37	43
8	7.7	11	14	15	18	29	33
9	3.5	6.1	7.2	7.6	10	15	18
10	3.8	6.0	7.0	7.5	9.2	18	20
11	3.0	4.7	5.7	6.1	6.2	15	19
12	2.6	3.8	4.3	4.4	5.9	15	17
13	1.8	2.7	3.0	2.8	3.9	7.9	8.9
14	2.1	2.5	2.7	2.4	2.8	6.2	7.4
15	1.5	1.6	1.6	.14	1.7	3.7	4.6

creasing fragment Z. Both components exhibit somewhat lower cross sections than for the ^{197}Au target over most of the energy range studied here.

In addition to providing a systematic overview of IMF emission between $E/A=20$ and 100 MeV bombarding energy, two distinct features of the excitation functions in Fig. 7 should be noted.

First, and most apparent, is the significant increase in $\sigma_{\text{IMF}}(Z)$ from the $^{\text{nat}}\text{Ag}$ target between $E/A=60$ and 80 MeV. In contrast, the variation of $\sigma_{\text{IMF}}(Z)$ for the ^{197}Au target is uniform across this region. The discontinuity in the $^{14}\text{N}+^{\text{nat}}\text{Ag}$ excitation function grows with increasing fragment charge and on the basis of the moving-source decomposition appears to be associated with the equilibrium component. The effect is apparent in the differential-cross-section data for the IMF's observed at 70° and 90°, where the spectra are well defined and kinematic shifts are minimal. These spectra are shown in Fig. 8. The distortion of the Coulomb peak toward lower energies exerts an important influence on the cross-section results for the Ag target at the highest energies (Fig. 4).

Since detector thresholds truncate the Coulomb peaks of the higher-Z spectra for $\theta\geq 120°$, we have investigated the possibility that instrumental cutoffs might generate the discontinuities observed in Fig. 7. The low-energy cross-section extrapolations for these angles depend on the moving-source fits, which are dominated by the equilibrium component for $\theta\geq 70°$ (see Fig. 1). For $8\leq Z\leq 15$ fragments, the systematic evolution of the spectra with angle constrains the fits strongly. This is due to two factors: (1) the distinct Coulomb peaks for the five angles with $\theta\leq 90°$ and (2) the uniform kinematic shifts of the spectral tails for the five backward angles with $\theta\geq 70°$. The fits predict backward-angle spectra that are self-consistent with the data for the $^{\text{nat}}\text{Ag}$ target at intermediate angles and the backward-angle data for the ^{197}Au target. In order to reduce the values of σ_{IMF}, it would be necessary to employ significantly larger Coulomb barriers at backward angles relative to the data for $\theta\leq 90°$. How-

TABLE V. Cross sections for IMF production from targetlike source, $\sigma_{\text{tot}}(Z)=\sigma_{\text{eq}}(Z)+\sigma_{\text{neq}}(Z)$, for the $^{14}\text{N}+^{197}\text{Au}$ reaction as a function of bombarding energy. Statistical plus systematic errors range from about 10% for $Z=3$ fragments to 20% for $Z=15$.

				E/A (MeV)			
$\sigma_{\text{tot}}(Z)$ (mb)	20	30	40	50	60	80	100
3	54	175	256	304	344	353	361
4	22	58	91	104	122	132	143
5	19	43	75	86	97	106	115
6	14	32	55	65	75	82	91
7	4.8	16	27	34	40	48	53
8	4.7	11	17	24	29	32	38
9	3.1	6.1	12	16	20	22	26
10	2.5	5.9	10	14	17	20	24
11	1.9	5.2	9.1	11	13	18	21
12	1.4	4.1	5.8	6.4	12	17	20
13					9	14	17
14					7.6	11	14
15					5.1	9.2	10

ever, if the unmeasured portion of the spectra is shifted and/or broadened toward lower energies than predicted by the fits, then our cross sections will be increased.

A possible explanation for the cross-section enhancement observed in Fig. 7 for the $^{\mathrm{nat}}$Ag target at energies above $E/A=60$ MeV may be the onset of multiple IMF decay processes from highly excited reaction residues. Evidence for such events has recently been reported in several coincidence studies [21,22,24,29] at total bombarding energies in excess of about 1 GeV. On the basis of linear-momentum-transfer systematics, discussed in Sec. V below, the average excitation energy per nucleon in these systems is somewhat lower than that for which multiple IMF decays are expected [26,27]. However, since the distribution of linear momentum transfers is quite broad in these reactions, the high-energy tail of the resulting excitation energy distribution (i.e., the most central collisions) may contain sufficient probability to account for the results. It should be noted that only 20–30 % of the reaction cross section results in IMF emission. Because the strongest cross-section enhancements are found for the low-yield heavy fragments, the increase in the total IMF emission probability is only about 10–15 %. Thus only 2–4 % of the reaction cross section is required to account for the observed results in terms of multiple IMF emission. Clearly, experiments of the 4π nature are essential to verify this interpretation.

The multiple fragment emission picture suggested above is also consistent with the energy spectra for Na fragments shown in Fig. 4. The broadening of the

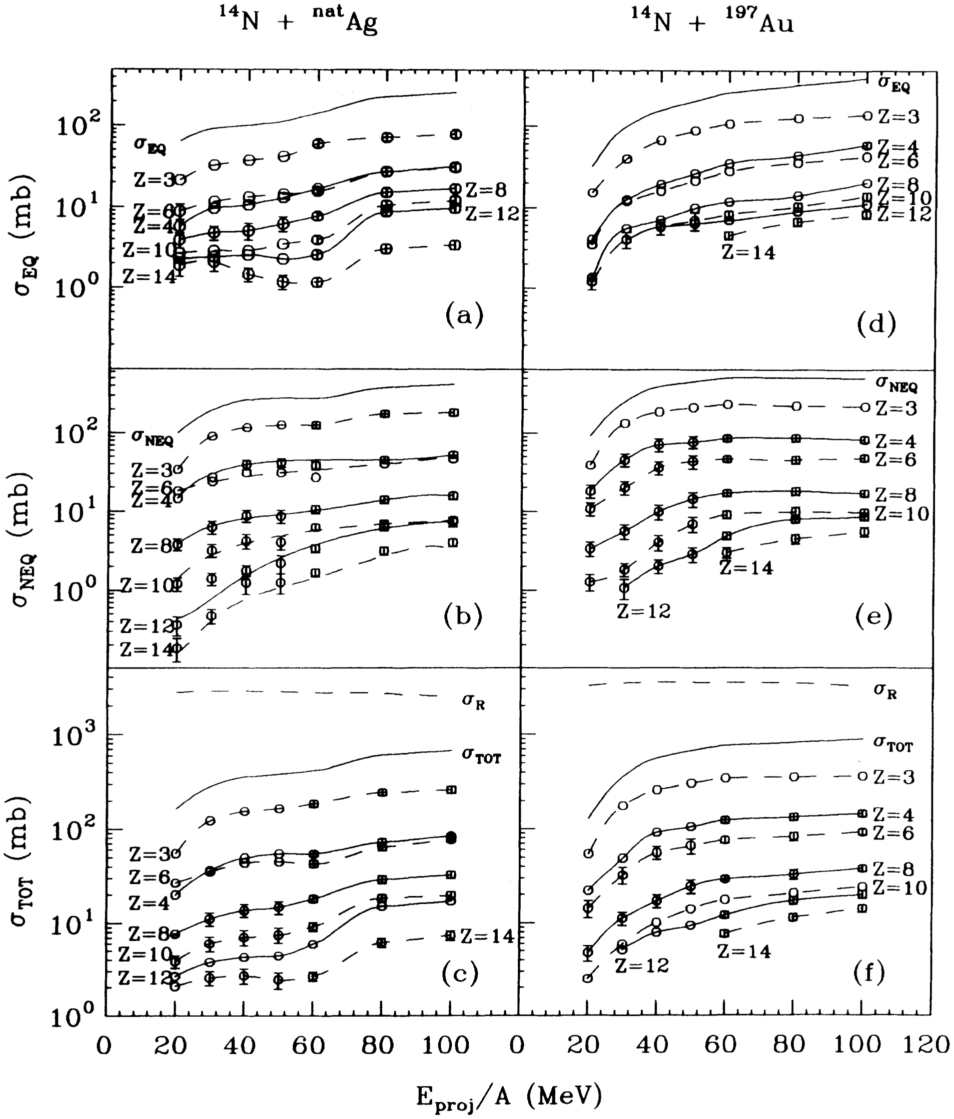

FIG. 7. Excitation functions for IMF's emitted in the ^{14}N+$^{\mathrm{nat}}$Ag (left column) and ^{14}N+^{197}Au (right column) reactions, as extracted from three-source fits. Data are shown for fragments with $Z=3$ and all even Z for the equilibrium (upper frames), nonequilibrium (middle frames), and the sum of these (bottom frames) sources. Also shown are total IMF cross sections σ_{IMF} for each case and for the total reaction cross section σ_R calculated according to Ref. [48]. Lines are to guide the eye. Representative error bars are shown in figure; other data behave similarly.

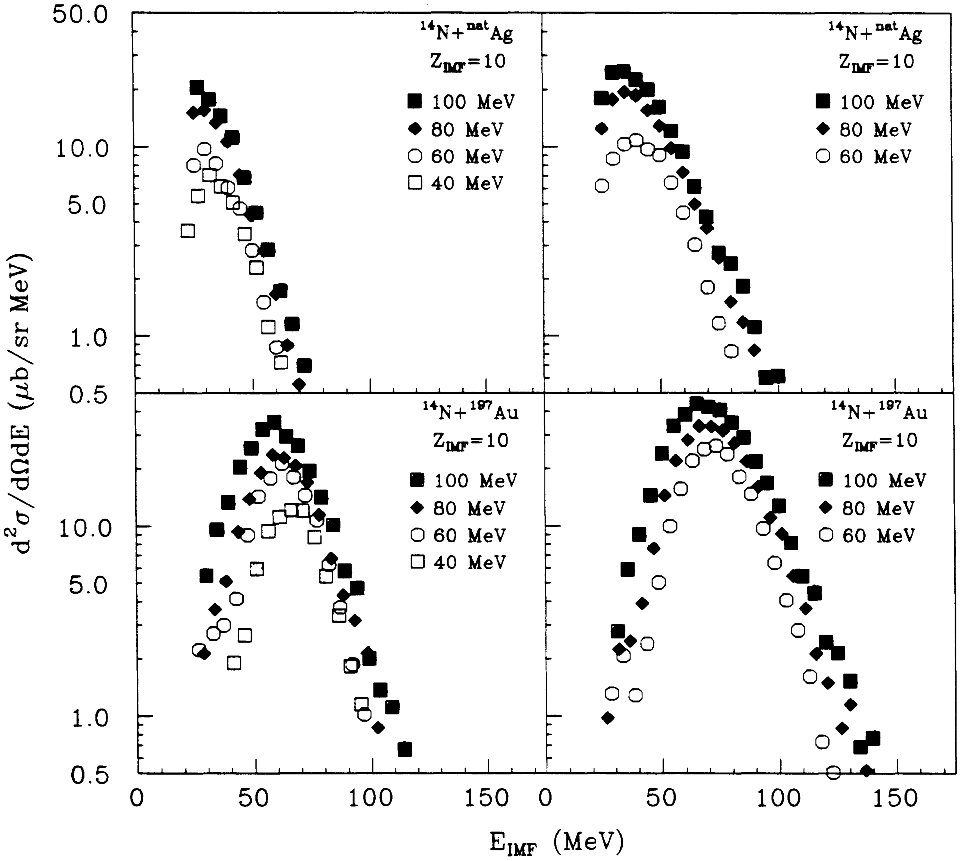

FIG. 8. Energy spectra for $Z=10$ fragments at 70° (right) and 90° (left) for the $E/A=40$, 60, 80, and 100 MeV ^{14}N+^{nat}Ag reaction (upper) and ^{14}N+^{197}Au (lower) reaction.

Coulomb peaks toward lower energies for the higher-bombarding-energy systems indicates emission from a system for which the Coulomb field has been modified significantly from that at lower energies. The question remains as to why both the excitation functions and fragment spectra are anomalous for ^{nat}Ag and not for ^{197}Au. As a simple gauge of the relative importance of very-high-excitation-energy processes, one can examine the bombarding energy corresponding to the total binding energy of the composite system. For ^{14}N+^{nat}Ag this value is $E/A\approx 80$ MeV, while for ^{14}N+^{197}Au it occurs near $E/A\approx 125$ MeV. Although one does not expect full projectile energy dissipation in these reactions, this indicator does scale with the excitation energy per nucleon of the composite system. On this basis the difference between the two targets is interpreted in terms of the excitation energy per nucleon in the ^{14}N+^{197}Au system being too low to produce significant multiple IMF emission.

A second important aspect of these data is the relative contribution of equilibrium and nonequilibrium IMF emission as a function of increasing projectile energy. The importance of nonequilibrium relative to total IMF emission from the targetlike source is plotted as a function of bombarding energy in Fig. 9 for light ($Z=4$) and heavy ($Z=10$) IMF's. Previously, analysis of our data below $E/A=50$ MeV ^{14}N energy [6] indicated that for high-Z IMF's ($Z\gtrsim 8$) nonequilibrium IMF emission increased rapidly with bombarding energy relative to equilibrium emission, suggesting that the former process might become dominant at higher energies. However, the present data do not support such a conclusion. For $E/A\geq 60$ MeV, the ratios of $\sigma_{eq}(Z)/\sigma_{tot}(Z)$ remain approximately constant, with nonequilibrium emission favoring lower-Z fragments and equilibrium emission favoring those with higher Z.

For both targets the behavior of the lightest IMF's is similar. Nonequilibrium emission dominates, but the ratio of nonequilibrium fragments to the total IMF yield decreases gradually from about 0.8 to 0.6 over the observed bombarding energy range. In the case of the heavier IMF's, nonequilibrium emission relative to the total yield increases rapidly at low energies, peaking at a value of about 0.5 in the vicinity of $E/A=40$–60 MeV, i.e., just beyond the Fermi energy. For the ^{nat}Ag target the decrease in $\sigma_{neq}/\sigma_{tot}$ at higher energies is the result of a growth in the yield of equilibriumlike fragments as the beam energy approaches the total binding energy, as is illustrated in Fig. 9. A similar effect may be present in the ^{197}Au data at $E/A=100$ MeV, although within the quoted errors this is not compelling.

It is also important to compare these IMF excitation functions with corresponding results for their heavy-residue partners. Heavy residues have been measured radiochemically and shown to account for a significant fraction of the cross section for bombarding energies above $E/A\gtrsim 50$ MeV [49]. Comparison of the summed

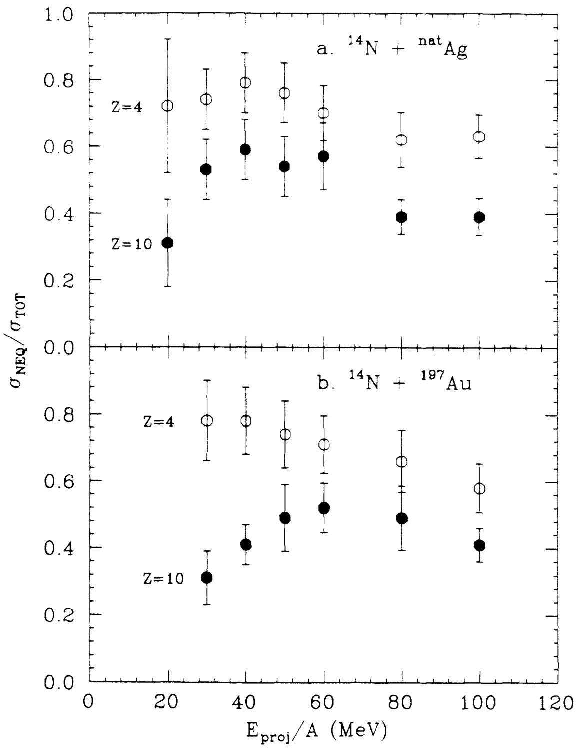

FIG. 9. Ratio of nonequilibrium (σ_{neq}) to total IMF cross sections ($\sigma_{eq}+\sigma_{neq}$) as a function of bombarding energy for the ^{14}N+^{nat}Ag reaction (upper frame) and ^{14}N+^{197}Au reaction (lower frame).

IMF yields for the ^{14}N+^{197}Au reaction (Table V and Fig. 7) with heavy-residue yields from the ^{12}C+^{197}Au reaction at similar energies shows that the IMF cross sections are comparable but slightly smaller than those for heavy residues in the complementary mass range. Since few nucleon transfers and multiple nucleon and α evaporation must necessarily account for at least part of the heavy-residue cross section, the observed results seem self-consistent.

The fragment charge distributions also carry information relevant to the mechanisms responsible for IMF formation. These data have been analyzed in terms of a power law [20]

$$\sigma(Z)\propto Z^{-\tau} ,$$

where the parameter τ is derived from a fit to the cross-section data in Tables IV and V. Values of τ obtained in this work are plotted as a function of bombarding energy in Fig. 10 for the equilibrium, nonequilibrium, and total charge distributions. Again, the two targets behave somewhat differently. For the ^{197}Au target the equilibrium charge distributions are essentially constant, yielding a value of $\tau=2.0\pm0.1$ over the entire range of bombarding energies. Values of $\tau\approx2$ have been used as evidence for a nuclear liquid-gas phase transition in high-energy proton-induced reactions [20]. However, the present data demonstrated that similar values can be obtained in simple statistical decay processes (e.g., the $E/A=20$ MeV ^{14}N+^{197}Au data), where angular momentum exerts an important influence on the fragment yields by enhancing heavy-fragment emission. The ^{nat}Ag target produces similar values of τ for the equilibrium component near threshold and at the highest bombarding energies; however, a maximum is observed near $E/A\approx50$ MeV. This behavior may be due to the fact that for the ^{14}N+^{nat}Ag system at low energies, the equilibrium IMF and fission components overlap in the data and cannot be easily separated. The low-Z tail of the fission cross section could enhance the cross section for $Z\geq10$, producing lower τ values. This problem is not as severe at higher bombarding energies because of the lower probability for fission relative to IMF emission.

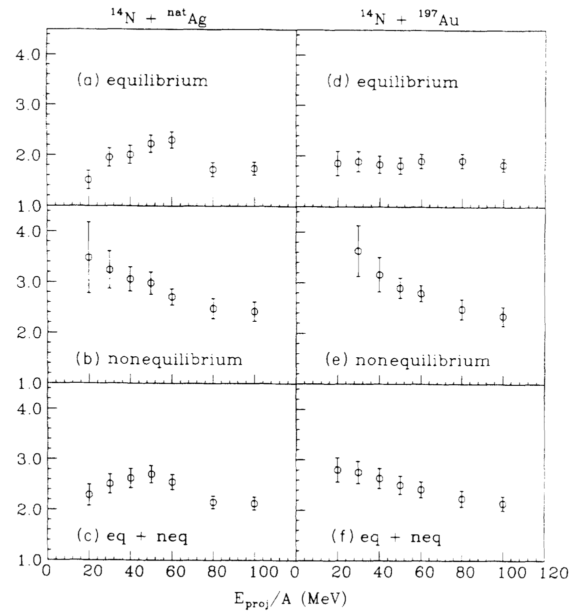

FIG. 10. Power-law exponents τ for IMF charge distributions as a function of bombarding energy in the reaction of ^{14}N with ^{nat}Ag (left column) and ^{197}Au (right column).

Nonetheless, differences in the charge distributions may serve to identify changes in the reaction mechanism. For example, several studies have shown that significantly larger values of τ are associated with nonequilibrium IMF's than for the equilibrium component [4,31,32,50]. This is demonstrated in the present data [Figs. 10(b) and 10(e)]. Here the τ values decrease monotonically for both targets from values near $\tau\approx3.5$ at the lowest energies to values slightly above $\tau\approx2$ at $E/A=100$ MeV. Thus, in ^{14}N-induced reactions, it appears that the τ values for equilibrium and nonequilibrium emission converge at high bombarding energies, similar to results observed in proton- and ^{3}He-induced reactions [31,32].

V. ENERGY DEPENDENCE OF SOURCE PARAMETERS

In order to examine the physics implications and self-consistency of the three-source fits described above, we present in this section the systematic behavior of the fit parameters as a function of ^{14}N energy. For most of the parameters, there is little dependence on IMF charge

[46], as demonstrated in the Appendix. This permits the use of average parameter values for each bombarding energy and target nucleus. These values are tabulated at Tables II and III.

First, the parameters which describe the equilibrium source are examined. In the top frame of Fig. 11, the ratio of the averages extracted source velocity, $\langle v_{\rm eq} \rangle$, to that of the composite system formed in a complete-fusion reaction, $v_{\rm CN}$, is plotted as a function of projectile energy. Averages have been taken over the IMF range $Z=3-15$ for each target; errors represent the standard deviation of the corresponding set of individual $v_{\rm eq}(Z)$ values, as shown in the Appendix. Near threshold the source velocities are approximately consistent with complete fusion for both projectile-target systems. As the beam energy increases, $\langle v_{\rm eq} \rangle / v_{\rm CN}$ decreases systemically below the complete-fusion expectation, consistent with the increasing probability for incomplete fusion and preequilibrium light-charged-particle emission prior to IMF emission [51,52].

Also plotted in Fig. 11 is the average value of $\langle v_{\rm eq} \rangle / v_{\rm CN}$ deduced from inclusive fission-fission angular correlation studies of the linear momentum transfer in the ^{14}N+^{238}U reaction [51,52], corrected for target-mass dependence according to the systematics of Batsch *et al.* [53] (solid line). The equilibrium IMF velocity ratios fall above the linear-momentum-transfer (LMT) results, which integrate over all IMF sources. This result indicates that, on average, IMF's are formed in more violent collisions, as expected on the basis of coincidence studies [5,54]. Comparing the values of $\langle v_{\rm eq} \rangle / v_{\rm CN}$ for the two targets, it is observed that the ratios for Ag are significantly lower than for ^{197}Au at the same value of E/A, implying a larger amount of missing momentum for the lighter target. This target-mass dependence has been previously reported [53] and is attributed to the increasing ratio of the diffuse surface to central density cross-sectional area presented to the beam for decreasing target-mass number.

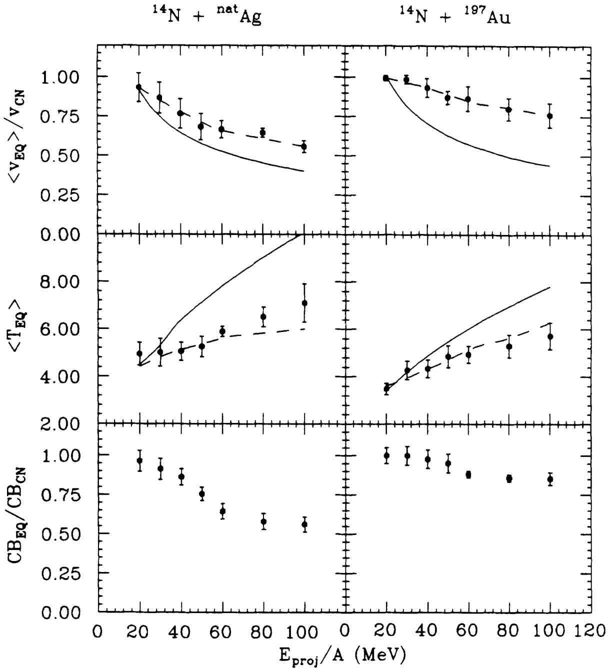

FIG. 11. Dependence of equilibrium velocity (top), temperature (middle), and Coulomb barrier (bottom) fit parameters (averages over $Z=3-15$) on bombarding energy for the ^{14}N+$^{\rm nat}$Ag system (left column) and ^{14}N+^{197}Au system (right column). Solid line on plot of $\langle v_{\rm eq} \rangle / v_{\rm CN}$ represents most probable linear momentum transfer systematics [51,52]; solid line on plot of $\langle T_{\rm eq} \rangle$ is the temperature for a fully equilibrated complete-fusion residue. Dashed line in top frame is average of data; this line is used to generate dashed line for $\langle T_{\rm eq} \rangle$ in middle frame, as described in text.

The middle frames of Fig. 11 show the average equilibrium temperatures $\langle T_{\rm eq} \rangle$ extracted from the fits as a function of projectile energy. For both systems the values of $\langle T_{\rm eq} \rangle$ increase with increasing projectile energy. Temperatures for the $^{\rm nat}$Ag target are significantly higher than for ^{197}Au, as expected for a Fermi gas with level-density parameter $a=A/{\rm const}\ {\rm MeV}^{-1}$. The solid line represents the calculated compound-nucleus temperatures ($T_{\rm CN}$) assuming complete fusion and $a=A/10$ MeV^{-1}. At low bombarding energies the temperatures are consistent with IMF emission from a fully equilibrated complete-fusion residue for both systems. With increasing beam energy the values of $\langle T_{\rm eq} \rangle$ fall systematically below the complete-fusion limit, reflecting the loss in internal excitation due to preequilibrium processes prior to IMF emission. For silver this deviation grows at nearly twice the rate as for the heavier ^{197}Au nucleus, in agreement with the momentum-transfer/excitation-energy loss implied by the ratio of $\langle v_{\rm eq} \rangle / v_{\rm CN}$.

Extracted temperatures for the equilibrium source extend up to 7.1 MeV for the $E/A=100$ MeV ^{14}N+$^{\rm nat}$Ag reaction, approaching the average nuclear binding energy for this system. However, interpreting $T_{\rm eq}$ as the actual temperature of the compound nucleus requires caution, since any nonequilibrium contributions to the spectra will lead to higher fit temperatures. Nonetheless, on the basis of the three-source fits performed here, the results at backward angles (Figs. 1–4) suggest that nonequilibrium contributions are small at angles greater than 120°.

In this regard it is interesting to note that the values of $\langle T_{\rm eq} \rangle$ extracted from the fits are consistent with the equilibrium temperatures implied by the experimental values of $\langle v_{\rm eq} \rangle / v_{\rm CN}$ in Fig. 11. The dashed line in the top frame of Fig. 11 represents the average value of $\langle v_{\rm eq} \rangle / v_{\rm CN}$, and that in the middle frame is the result of a calculation in which $\langle v_{\rm eq} \rangle$ is used to estimate the excitation energy of the residual nucleus. For this purpose a simple incomplete-fusion model is assumed in which the missing momentum is carried off by beam velocity nucleons. No account is made for Q-value effects or preequilibrium emission. The former effect is small at these bombarding energies. The latter is significant, but difficult to assess; it has the net effect of raising the excitation energy and therefore the corrected temperatures of the residual nucleus, given by the dashed curve in Fig. 11. In general, the comparisons between the calculation and experimental values of $T_{\rm eq}$ are in relatively good agreement, within the limits of error of the data and the uncertainties of the incomplete-fusion model.

Values for the Coulomb barriers relative to those expected from fission systematics [55] (corrected for mass asymmetry) are shown in the bottom frame of Fig. 11. For most of the projectile energy range, the extracted Coulomb barriers are close to those expected from fission systematics. However, there is a steady decrease in the ratio $B_{\rm eq}/B_{\rm CN}$ as a function of increasing ^{14}N energy. This reduction is most pronounced for IMF emission from the $^{\rm nat}$Ag target above beam energies of $E/A=50$ MeV and appears similar to distortions of the Coulomb peak toward lower energies observed in the other systems [10,20,29,31]. The remaining two equilibrium-fit parameters—which account for spectral shape and angular anisotropy—show a distinct dependence on fragment charge, but little systematic variation with bombarding energy. These are discussed in the Appendix.

The extracted parameters for the nonequilibrium IMF source are presented in Fig. 12. The ratio of the average source velocity to that of the beam, $\langle v_{\rm neq}\rangle/v_{\rm beam}$, is shown in the top frame of Fig. 12 as a function of bombarding energy. For both targets the results are similar, yielding ratios which decrease from $\langle v_{\rm neq}\rangle/v_{\rm beam}\approx 0.30-0.35$ at $E/A=20$ MeV to $\langle v_{\rm neq}\rangle/v_{\rm beam}\approx 0.10-0.15$ at the highest projectile energy. Since the beam velocity increases by about a factor of 2 over this energy region, this result implies an approximately constant velocity for the average nonequilibrium source $\langle v_{\rm neq}\rangle\approx 0.06c$ (solid line). The extracted velocity ratios are somewhat lower than most previous moving-source fits to the nonequilibrium component, which have favored values of $v_{\rm neq}/v_{\rm beam}\approx 0.3-0.5$. This is accounted for primarily by three factors: (1) our use of a forward-peaked nonequilibrium source, which provides much better agreement with the spectra than an isotropic source; (2) the low detector thresholds and extensive backward angle coverage that permit a much better definition of the equilibrium component, enhancing $\sigma_{\rm eq}$ relative to $\sigma_{\rm neq}$; and (3) the inclusion of a projectilelike source at forward angles.

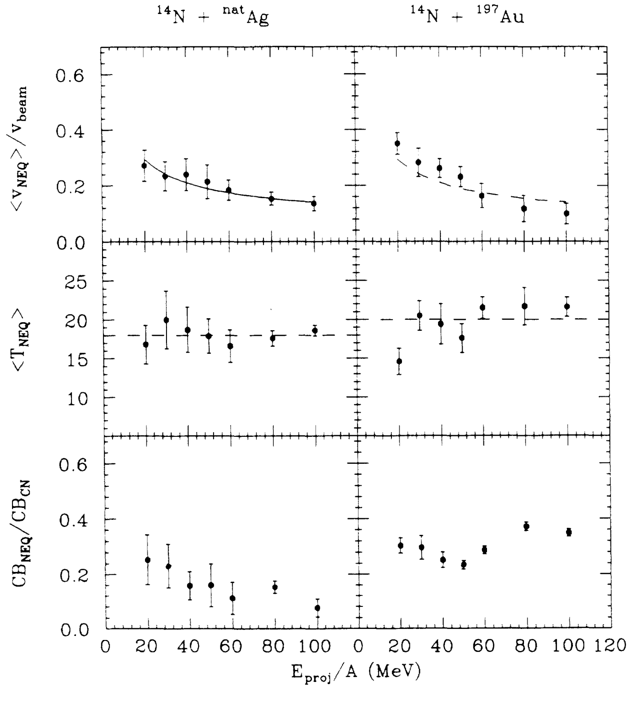

FIG. 12. Dependence of nonequilibrium velocity (top), temperature (middle), and Coulomb barrier (bottom) fit parameters, averaged over $Z=3-15$, on bombarding energy for the ^{14}N+$^{\rm nat}$Ag system (left column) and ^{14}N+^{197}Au system (right column). Solid line on plot of $\langle v_{\rm neq}\rangle/v_{\rm beam}$ is for $v_{\rm neq}=0.060c$, and dashed line on $\langle T_{\rm neq}\rangle$ is the average value for all bombarding energies.

The slope parameters $T_{\rm neq}$ are shown in the middle frame of Fig. 12, and the values of $\langle T_{\rm neq}\rangle$ are found to be essentially independent of bombarding energy above $E/A=30$ MeV. For the $^{\rm nat}$Ag target all values are consistent with $T_{\rm neq}\approx 18$ MeV, and for gold we find $T_{\rm neq}\approx 20$ MeV (excluding the point at $E/A=20$ MeV, where nonequilibrium yields are poorly defined). Similar results have been observed by Trockel *et al.* [12] for ^{16}O-induced reactions. In addition, a bombarding-energy independence has been reported for the slope parameters associated with pion spectra from heavy-ion-induced reactions in the energy range $E/A\cong 30-100$ MeV, where values of $T_\pi\cong 20-22$ MeV are found [56]. In contrast, a distinct dependence of $T_{\rm neq}$ on bombarding energy over this same energy range has been reported in Ref. [46] for light-charged particles (LCP's) and IMF's emitted in $E/A=42-151$ MeV Ne- and Ar-induced reactions on ^{197}Au. The fitting procedure in Ref. [46] employed a single isotropic emission source, and the detector configuration emphasized forward-angle IMF emission with detector thresholds of $E/A\approx 3-5$ MeV. To illustrate the sensitivity of $T_{\rm neq}$ for the IMF component to the completeness of the data set, Fig. 13 shows values of $T_{\rm neq}$ for fits to our data performed over the angular range ($30^\circ\le\theta\le 130^\circ$) with detector thresholds for IMF's of $E/A=4$ MeV, identical to those in the measurements of Ref. [46]. Here one observes a systematic increase in $T_{\rm neq}$ with bombarding energy, in contrast to the energy-independent values of $T_{\rm neq}$ derived from the full data set. These results emphasize that extracted nonequilibrium temperature parameters are dependent upon the experimental conditions under which the data were obtained. Data taken over a limited angular range or with thresholds well above Coulomb energy do not adequately account for equilibrium emission and thereby produce anomalous values of $T_{\rm neq}$.

It is also of interest to compare the spectral values of $T_{\rm neq}$ with temperatures obtained with the population-of-excited-states method for similar systems. For the $E/A=35$ MeV ^{14}N+^{197}Au and $E/A=^{16}$O+^{197}Au reactions, temperatures of 4–5 MeV were deduced in Ref. [57]. While these values are much lower than the values of $T_{\rm neq}\approx 20$ MeV from the moving-source fits, they are closer to the values of $T_{\rm eq}$ determined for the equilibrium temperature. These results highlight the difficulty in evaluating the thermal/temporal characteristics of nonequilibrium IMF's with simple models, such as that employed here.

Finally, the Coulomb barriers required to fit the nonequilibrium component are the order of 0.15–0.40 times

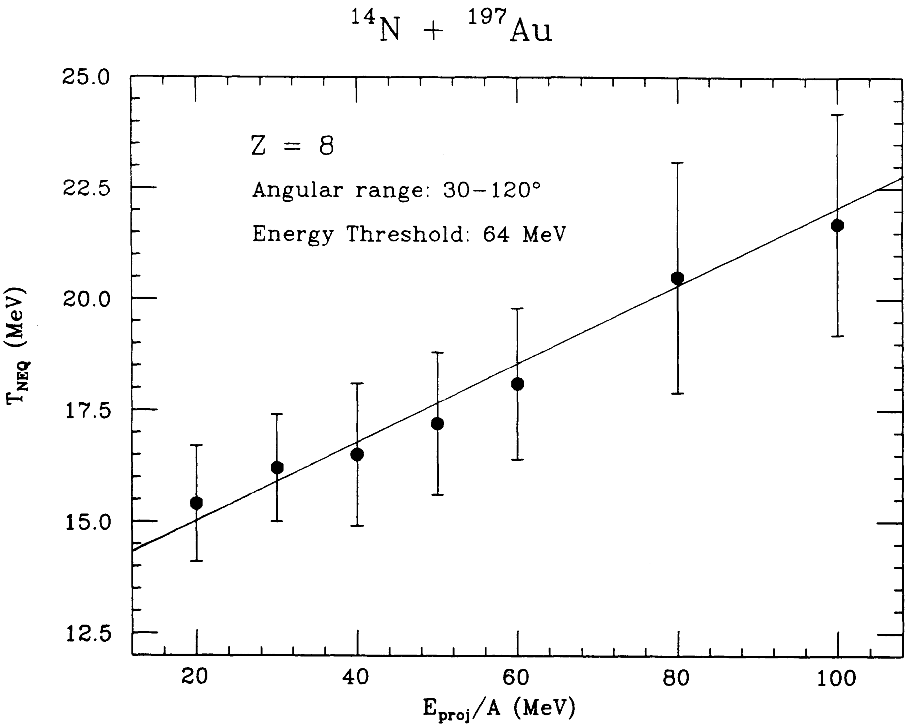

FIG. 13. Values of T_{neq} for $Z=8$ fragments from the $^{14}N+^{197}Au$ reaction as a function of bombarding energy. Fit is performed over angular region $30° \leq \theta \leq 130°$ and with a detector threshold $(E/A)_{IMF}=4$ MeV.

the barriers predicted by fission systematics [55] and are nearly independent of bombarding energy, as shown in the bottom frames of Fig. 12. This result coincides with previous studies that have shown small Coulomb barriers for nonequilibrium fragment emission [4–12].

VI. CONCLUSIONS

In summary, excitation functions have been measured for intermediate-mass fragments formed in the reaction of $E/A=20-100$ MeV ^{14}N ions with targets of ^{nat}Ag and ^{197}Au. The IMF energy spectra and angular distributions are found to be well described by a moving-source model parametrized by three sources: (1) statistical decay of equilibrated compound nuclei, (2) nonequilibrium emission from a composite source which retains only the directional memory of the projectile, and (3) projectile remnants from direct transfer processes, partially damped collisions, and projectile fragmentation. Although this decomposition oversimplifies the continuum of actual processes that produce IMF's, it provides the useful basis for examining the systematic properties of the data.

The excitation functions for both targets show a rapid rise in IMF probability at low energies, followed by a gradual increase thereafter. One of the most striking features of the data is that above $E/A=20$ MeV, the spectra for a given IMF are nearly independent of bombarding energy. The total IMF cross sections are observed to be significantly smaller than the total reaction cross sections over this entire bombarding energy region, although the ratio σ_{IMF}/σ_R continues to rise up to the maximum energy studied, $E/A=100$ MeV, where values near 25–30% of σ_R are observed. If a significant fraction of these events are from multiplicities greater than 1, this ratio will be smaller. For energies beyond the Fermi energy, the equilibrium and nonequilibrium cross sections are roughly equal in magnitude; light fragments are enhanced in the nonequilibrium yields and heavy fragments in the equilibriumlike yields.

The excitation functions for the $^{14}N+^{nat}Ag$ reaction show evidence for a significant increase in IMF probability for $E/A>60$ MeV. One possible explanation for this increase in cross sections is that multiple IMF emission may be enhanced for projectile energies comparable to the total nuclear binding energy. These results also show a more rapid growth for nonequilibrium emission from the ^{nat}Ag target relative to ^{197}Au. This may be related to the greater average transparency for IMF's formed in the ^{nat}Ag nucleus relative to ^{197}Au.

Examination of the charge distributions in terms of a power-law analysis shows that for the equilibrium component the power-law exponent τ remains nearly constant at a value of $\tau \approx 2.0 \pm 0.2$. In contrast, nonequilibrium emission is characterized by τ values that decrease from $\tau \approx 3.5$ near threshold to values near those for equilibrium emission at $E/A=100$ MeV, similar to the behavior observed in light-ion-induced reactions [31,32].

The source parameters for the velocity, temperature, and Coulomb barrier extracted from the fitting routines are found to be approximately independent of fragment charge [46]. The average equilibriumlike source velocities relative to those expected for complete fusion decrease systematically as a function of increasing beam energy. The ratio $\langle v_{\mathrm{eq}} \rangle / v_{\mathrm{CN}}$ exhibits an energy dependence which resembles that inferred from linear-momentum-transfer studies [51,52]. However, the values obtained here are somewhat higher in magnitude. This behavior is expected since the equilibrium source presumably arises from central collisions for which the momentum transfer is higher than average. The equilibrium source temperatures increase monotonically with beam energy, reaching a value of $T_{\mathrm{eq}} \cong 7$ MeV for the $^{14}\mathrm{N}+{}^{\mathrm{nat}}\mathrm{Ag}$ system at $E/A = 100$ MeV. This increase in temperature, however, is less than expected for a fully equilibrated complete-fusion residue, indicating that with increasing beam energy, there is a growing amount of linear momentum (and corresponding excitation energy) loss due to fast preequilibrium neutron and LCP emission.

Rather surprisingly, the average velocities for the nonequilibrium source are found to be nearly constant at $\langle v_{\mathrm{neq}} \rangle \approx 0.66c$ for both targets, independent of bombarding energy. Similarly, the spectral slope parameters extracted from the fits are approximately independent of target and bombarding energy at $T_{\mathrm{neq}} \approx 18$ MeV for $^{\mathrm{nat}}\mathrm{Ag}$ and 20 MeV for $^{197}\mathrm{Au}$. The variance of these results from Ref. [46] stresses the sensitivity of the moving-source fit parameters to both experimental conditions (detector thresholds, angular coverage, etc.) and the specific choice of parametrization used, e.g., number of sources employed, angular distribution assumptions, volume versus surface emission, etc. The present study demonstrates that measurements which provide maximum angular coverage and low detector thresholds are essential to account for the properties of complex fragment emission at intermediate energies.

ACKNOWLEDGMENTS

We wish to acknowledge Peter Miller and the NSCL operating crew for their efforts in providing beams for this study. We also thank Dave Sanderson of NSCL for his assistance with the 92-in. scattering chamber, Bill Lozowski of IUCF for fabricating the excellent high-purity targets, Ron Fox for electronics and computer support at NSCL, and John Dorsett of IU for construction of the detector telescope housings. This work was supported by DOE Grant No. DE-FG02-88ER.40404.A000 and NSF Grants No. PHY-87-14406 and No. PHY-89-13813.

APPENDIX: Z-DEPENDENT FIT PARAMETERS

In Sec. V several of the fitting parameters from the moving-source fits were discussed in terms of their average behavior. Here we present the fitting results for individual IMF Z values from $Z=3$ to 15, obtained at several energies with both targets (see also Ref. [46]). The squares represent data obtained for the $^{14}\mathrm{N}+{}^{197}\mathrm{Au}$ reaction, whereas the solid circles represent data for the $^{14}\mathrm{N}+{}^{\mathrm{nat}}\mathrm{Ag}$ system.

The equilibrium-source fit parameters are shown in Figs. 14–18 for the velocity ratio $v_{\mathrm{eq}}/v_{\mathrm{CN}}$, temperature T_{eq}, Coulomb barrier ratio $B_{\mathrm{eq}}/B_{\mathrm{CN}}$, amplification pa-

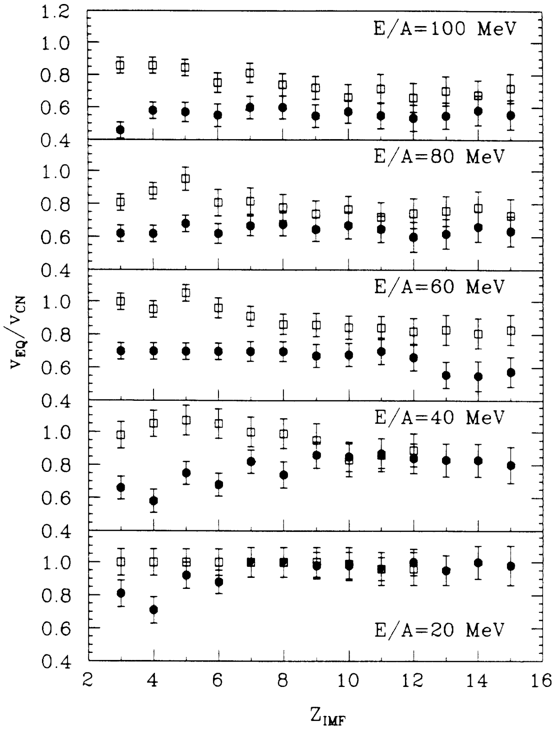

FIG. 14. Ratio $v_{\mathrm{eq}}/v_{\mathrm{CN}}$ as a function of IMF charge for the $E/A=20$, 40, 60, 80, and 100 MeV $^{14}\mathrm{N}+{}^{\mathrm{nat}}\mathrm{Ag}$ reaction (solid points) and $^{14}\mathrm{N}+{}^{197}\mathrm{Au}$ reaction (open points).

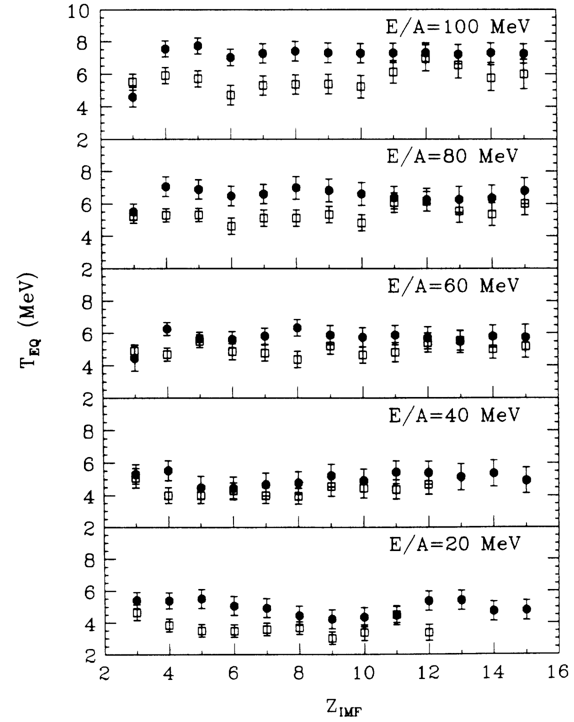

FIG. 15. Equilibrium temperature as a function of IMF charge for the $E/A=20$, 40, 60, 80, and 100 MeV $^{14}\mathrm{N}+{}^{\mathrm{nat}}\mathrm{Ag}$ reaction (solid points) and $^{14}\mathrm{N}+{}^{197}\mathrm{Au}$ reaction (open points).

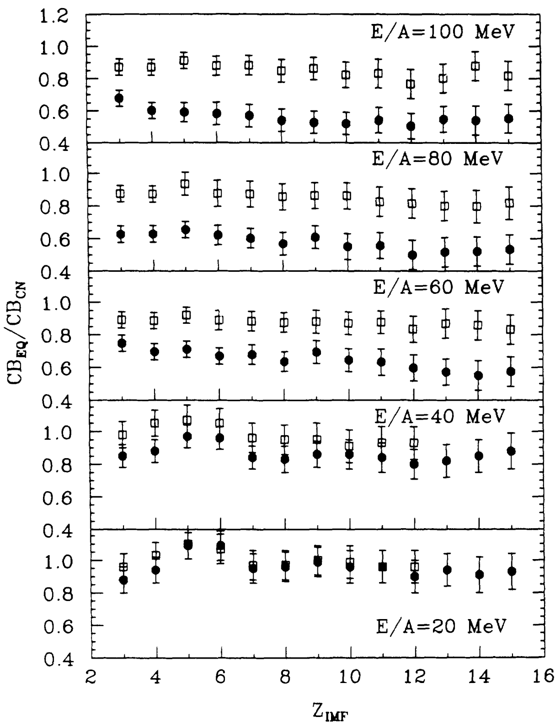

FIG. 16. Ratio of Coulomb barrier to that predicted by fission systematics as a function of IMF charge for the $E/A = 20$, 40, 60, 80, and 100 MeV $^{14}N + {}^{nat}Ag$ reaction (solid points) and $^{14}N + {}^{197}Au$ reaction (open points).

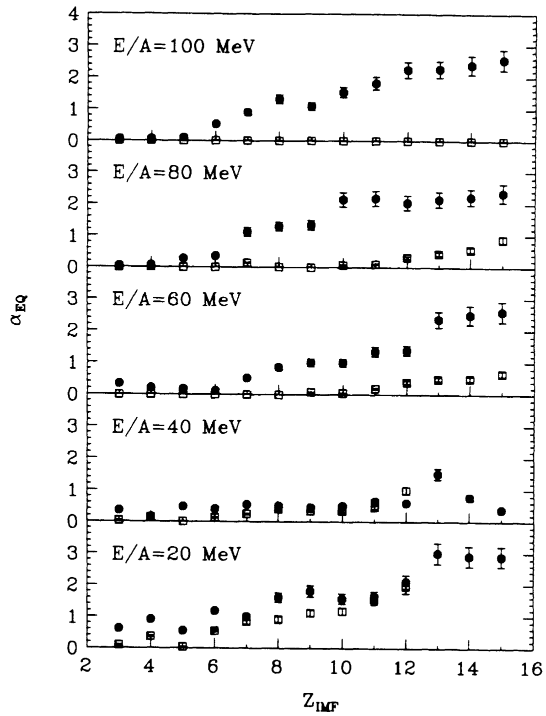

FIG. 18. Anisotropy parameter for equilibrium source as a function of IMF charge for the $E/A = 20$, 40, 60, 80, and 100 MeV $^{14}N + {}^{nat}Ag$ reaction (solid points) and $^{14}N + {}^{197}Au$ reaction (open points).

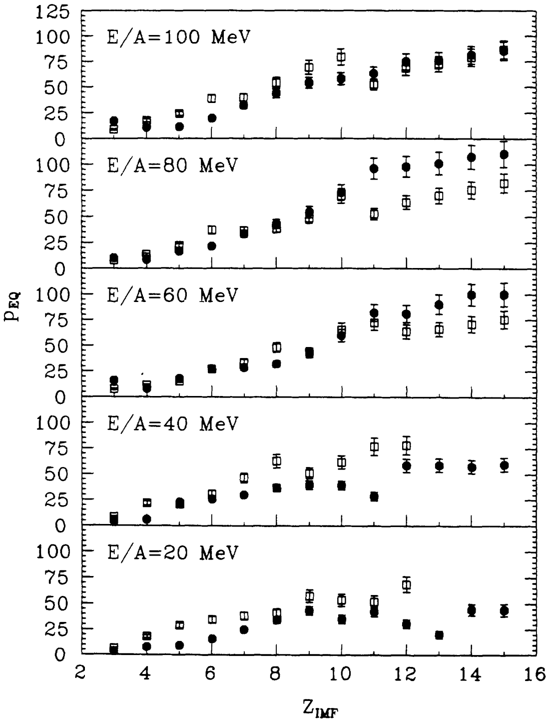

FIG. 17. Spectral shape parameter p for equilibrium source as a function of IMF charge for the $E/A = 20$, 40, 60, 80, and 100 MeV $^{14}N + {}^{nat}Ag$ reaction (solid points) and $^{14}N + {}^{197}Au$ reaction (open points).

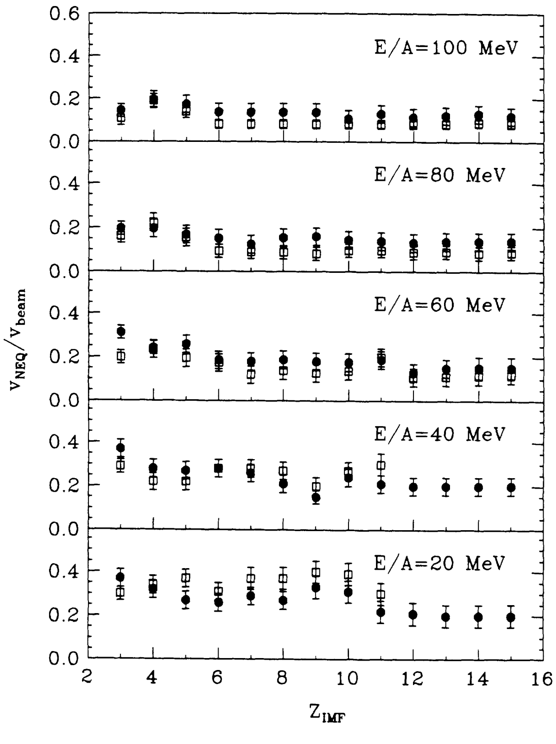

FIG. 19. Ratio of nonequilibrium source velocity to that of beam as a function of IMF charge for the $E/A = 20$, 40, 60, 80, and 100 MeV $^{14}N + {}^{nat}Ag$ reaction (solid points) and $^{14}N + {}^{197}Au$ reaction (open points).

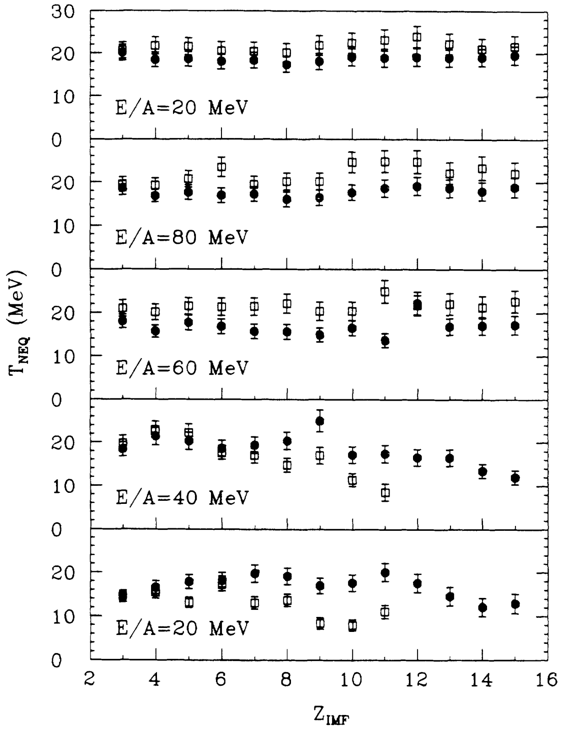

FIG. 20. Nonequilibrium-source temperature as a function of IMF charge for the $E/A = 20$, 40, 60, 80, and 100 MeV $^{14}N + ^{nat}Ag$ reaction (solid points) and $^{14}N + ^{197}Au$ reaction (open points).

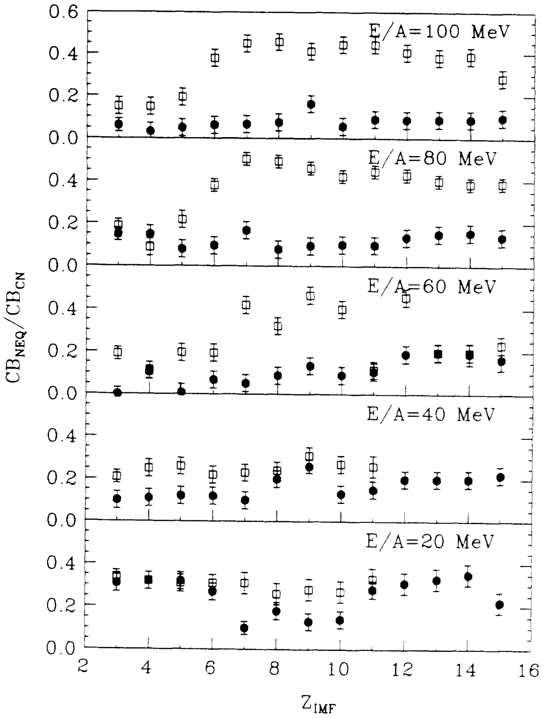

FIG. 21. Ratio of Coulomb barrier for nonequilibrium source B_{neq} to that based on fission systematics as a function of IMF charge for the $E/A = 20$, 40, 60, 80, and 100 MeV $^{14}N + ^{nat}Ag$ reaction (solid points) and $^{14}N + ^{197}Au$ reaction (open points).

rameter p_{eq}, and anisotropy parameter α_{eq}, respectively. Except at the lowest bombarding energies, where the lightest fragments appear to have somewhat lower velocities, the velocity ratios are seen to be constant within statistical errors. The gradual increase in missing momentum (reflected by $v_{eq} < v_{CN}$) with increasing bombarding energy is apparent (see Fig. 11). Similar behavior is observed for the equilibrium temperatures and Coulomb barriers. With respect to the values of T_{eq}, consistent values between 7 and 8 MeV are required to fit the data at $E/A = 100$ MeV. For lower energies these decrease systematically as discussed in Sec. V. The spectral shape parameters p_{eq} are found to be strongly Z dependent, ranging from values of 5 to 10 for low Z values to between 50 and 100 for $Z = 14$. While these values are in general agreement with previous analyses, the fits at higher bombarding energies produce somewhat larger values than usually reported. Finally, the anisotropy parameters α_{eq} are also Z dependent, as would be expected for a fissionlike process. Forward-backward anisotropies (e.g., Fig. 5) are found at all bombarding energies and serve to increase the equilibrium cross sections relative to fitting procedures which do not include this angular momentum effect.

The nonequilibrium-source parameters are summarized in Figs. 19–21. The source velocity ratios with respect to the beam, v_{neq}/v_{beam}, appear in Fig. 19. While there is a tendency for the lower Z values to have slightly higher source velocities, the overall effect is small. The decrease in this average ratio with increasing projectile energy, shown in Fig. 12, is apparent. Slope "temperature" parameters for the nonequilibrium source are presented in Fig. 20. No clear dependence on IMF charge or projectile energy is observed in this plot, as noted in the text. Again, we reiterate these results are the product of a global three-source fitting routine to all spectra at all angles. The constancy of these T_{neq} values cannot be altered without major changes in the character of the other sources, especially that for equilibrium emission, which is found to be in good agreement with other studies. Values of the Coulomb parameter B_{neq}/B_{CN} in Fig. 21 behave more erratically than the other nonequilibrium source parameters. However, as long as this ratio is less than ~ 0.3, the fits are not very sensitive to the value of B_{neq}. Finally, the nonequilibrium angular distribution parameter b (not shown here), spans a range of values from about $b = 10-30$ degr^{-1}, with no systematic correlations with projectile energy or fragment charge.

The error analysis for the data from the moving-source fits was performed in three stages. First, the simultaneous fits were performed on an element-by-element basis. The upper and lower bounds for the fit parameters were determined by the amount of variation required to increase the value of χ^2 by 1.0 from its minimum value. Second, these upper and lower parameter values were put back into the fit equations to determine their effect on the cross sections derived from the fits. This stage provided first-order error bars for the derived cross sections. Finally, the fit parameters were adjusted manually in order to produce any fit that represented the data reasonably well. If the resulting upper and lower bounds for the derived cross sections were higher than those determined in the previous stage, then the error bars were increased to accommodate the new values. The third stage was performed mainly to determine the error introduced in extrapolating the fits back to IMF energies that were below the detector thresholds. The error bars from the third stage rarely contributed to the total as they were usually much lower than the error bars derived from the second stage. This fact should be evident from an examination of Figs. 5 and 6, where the nonextrapolated data are compared to the extrapolated fit results. Clearly, most of the cross section is represented in the measured energy range. Error bars determined from the above-described process (represented in Figs. 7–9) are believed to be overestimations of the true systematic and statistical errors. In several figures (Figs. 11–14), parameters that have been averaged over all elements are presented. In these figures the error bars represent the simple standard deviation from the mean parameter values for each Z.

[1] L. G. Sobotka *et al.*, Phys. Rev. Lett. **51**, 2187 (1983).
[2] W. A. Friedman and W. G. Lynch, Phys. Rev. C **28**, 16 (1983); **28**, 950 (1983).
[3] M. A. McMahan *et al.*, Phys. Rev. Lett. **54**, 1995 (1985).
[4] K. Kwiatkowski, J. Bashkin, H. Karwowski, M. Fatyga, and V. E. Viola, Phys. Lett. B **171**, 41 (1986).
[5] M. Fatyga *et al.*, Phys. Rev. Lett. **58**, 2527 (1987).
[6] D. E. Fields *et al.*, Phys. Lett. B **220**, 356 (1989).
[7] R. E. L. Green and R. G. Korteling, Phys. Rev. C **22**, 1594 (1980).
[8] D. J. Fields *et al.*, Phys. Rev. C **30**, 1912 (1984).
[9] C. B. Chitwood *et al.*, Phys. Lett. **131B**, 289 (1983); **152B**, 443 (1985).
[10] A. M. Poskanzer, G. W. Butler, and E. K. Hyde, Phys. Rev. C **3**, 882 (1971); E. K. Hyde, G. M. Butler, and A. M. Poskanzer, *ibid.* **4**, 1159 (1971).
[11] B. V. Jacak *et al.*, Phys. Rev. Lett. **51**, 1846 (1983).
[12] R. Trockel *et al.*, Prog. Part. Nucl. Phys. **15**, 225 (1985).
[13] M. Fatyga *et al.*, Phys. Lett. B **185**, 321 (1987).
[14] R. G. Stokstad, Comments Nucl. Part. Phys. **13**, 231 (1984).
[15] M. Burgel, H. Fuchs, H. Homeyer, G. Ingold, U. Jahnke, and G. Toma, Phys. Rev. C **36**, 90 (1987).
[16] V. Viola and K. Kwiatkowski, in *Proceedings of the Symposium: Towards a Unified Picture of Nuclear Dynamics,* edited by S. M. Lee and F. Sakata, AIP Conf. Proc. No. 250 (AIP, New York, 1991).
[17] A. I. Warwick *et al.*, Phys. Rev. C **27**, 1083 (1983).
[18] B. Jakobsson, G. Jönsson, L. Karlsson, B. Norén, K. Söderström, F. Schussler, and E. Mannard, Nucl. Phys. **A488**, 251c (1988).
[19] B. V. Jacak, Nucl. Phys. **A488**, 319c (1988).
[20] N. T. Porile *et al.*, Phys. Rev. C **39**, 1914 (1989); A. S. Hirsch *et al.*, *ibid.* **29**, 508 (1984); J. E. Finn *et al.*, Phys. Rev. Lett. **49**, 1321 (1982).
[21] S. J. Yennello *et al.*, Phys. Rev. Lett. **67**, 671 (1991).
[22] Y. D. Kim *et al.*, Phys. Rev. Lett. **63**, 494 (1989).
[23] R. Trockel *et al.*, Phys. Rev. C **39**, R729 (1989).
[24] J. B. Natowitz, in Proceedings of the International Conference on Nucleus-Nucleus Collisions, Kanazawa, Japan, 1991, edited by H. Toki and I. Tanihata [Nucl. Phys. (to be published)].
[25] M. Louvel *et al.*, in [16].
[26] W. G. Lynch, Annu. Rev. Nucl. Sci. **37**, 493 (1987).
[27] *Proceedings of the Symposium on Nuclear Dynamics and Disassembly,* Dallas, TX, 1989, edited by J. B. Natowitz (World Scientific, Singapore, 1989).
[28] C. K. Gelbke and D. H. Boal, Prog. Part. Nucl. Phys. **19**, 33 (1987).
[29] W. Trautman, in [16].
[30] N. M. Papadakis *et al.*, Phys. Lett. B **240**, 317 (1990).
[31] S. J. Yennello *et al.*, Phys. Lett. B **246**, 26 (1990).
[32] S. J. Yennello, K. Kwiatkowski, S. Rose, L. W. Woo, S. H. Zhou, and V. E. Viola, Phys. Rev. C **41**, 79 (1990).
[33] D. R. Bowman *et al.*, Nucl. Phys. **A523**, 386 (1991).
[34] J. L. Wile *et al.*, Phys. Lett. B **264**, 26 (1991).
[35] K. Kwiatkowski *et al.*, Nucl. Instrum. Methods **299**, 166 (1990).
[36] R. N. Yoder, Indiana University Cyclotron Facility Technical Report No. 85-4, 1985; C. R. Gould and N. R. Roberson, IEEE Trans. Nucl. Sci. **NS-30**, 3758 (1985).
[37] A. Kiss, F. Déak, Z. Seres, G. Caskey, A. Galonsky, B. Remington, and L. Heilbronn, Nucl. Phys. **A499**, 131 (1989).
[38] T. C. Awes *et al.*, Phys. Rev. C **24**, 89 (1981).
[39] B. B. Back *et al.*, Phys. Rev. C **22**, 1927 (1980).
[40] M. Blann, Annu. Rev. Nucl. Sci. **25**, 123 (1975).
[41] J. R. Wu, C. C. Chang, and H. D. Holmgren, Phys. Rev. C **19**, 370 (1979); **19**, 659 (1979).
[42] C. Volant, Y. Cassagnou, M. Conjeaud, R. Dayras, S. Harar, R. Legrain, and E. C. Pollacco, in Proceedings of the 3rd International Conference on Nucleus-Nucleus Collisions, University of Caen, Caen, France, 1988 (unpublished), p. 100.
[43] J. R. Nix, Ann. Phys. (N.Y.) **41**, 52 (1967).
[44] L. G. Moretto, Nucl. Phys. **A247**, 211 (1975).
[45] G. D. Westfall *et al.*, Phys. Rev. C **17**, 1368 (1978).
[46] B. V. Jacak *et al.*, Phys. Rev. C **35**, 1751 (1987).
[47] B. Borderie *et al.*, Phys. Lett. B **205**, 26 (1988).
[48] S. Kox *et al.*, Nucl. Phys. **A420**, 162 (1984).
[49] W. Loveland, K. Aleklett, L. Sihver, Z. Xu, C. Casey, and G. T. Seaborg, Nucl. Phys. **A471**, 175c (1987).
[50] W. Trautman *et al.*, in *Proceedings of the Symposium on Nuclear Dynamics and Nuclear Disassembly,* edited by J. B. Natowitz (World Scientific, Singapore, 1989), p. 365.
[51] M. B. Tsang *et al.*, Phys. Lett. **143B**, 169 (1984).
[52] M. Fatyga *et al.*, Phys. Rev. Lett. **55**, 1376 (1985).
[53] T. Batsch *et al.*, Phys. Lett. B **189**, 287 (1987).
[54] K. Arnold *et al.*, Hahn-Meitner Institute Berlin Annual Report No. HMI-B 490, 1990, p. 62.
[55] V. E. Viola, M. L. Walker, and K. Kwiatkowski, Phys. Rev. C **31**, 706 (1985).
[56] T. Suzuki, in [24].
[57] Z. Chen *et al.*, Phys. Rev. C **36**, 2297 (1987).